Skyrmionic Schrödinger cat states in monoaxial chiral magnets

Štefan Liščák,[*,†] Andreas Haller,[†] Andreas Michels, Thomas L. Schmidt, and Vladyslav M. Kuchkin
Department of Physics and Materials Science, University of Luxembourg, L-1511 Luxembourg, Luxembourg

(Received 21 May 2025; revised 16 October 2025; accepted 7 April 2026; published 12 May 2026)

We study the low-energy excitation spectra of a spin-1/2 quantum Heisenberg model with a monoaxial Dzyaloshinskii-Moriya interaction. Using the density matrix renormalization group method, our analysis reveals a degeneracy between skyrmion and antiskyrmion states, enabling the formation of a Schrödinger cat state, a quantum superposition of these topologically distinct textures. To characterize this nontrivial state, we compute two-point spin correlation functions, highlighting signatures accessible via neutron scattering experiments. Furthermore, we demonstrate that applying a magnetic field gradient induces a coherent time evolution of the cat state, offering a controllable mechanism for its manipulation. These findings provide a framework for the detection of skyrmionic Schrödinger cat states in quantum magnets.

DOI: 10.1103/842q-ghyt

I. INTRODUCTION

Two-dimensional skyrmions are topological solitons with particlelike properties, holding significant potential for applications in spintronics [1], magnetic memory recording, neuromorphic computing [2], and quantum computing [3–6]. Initially, skyrmions were studied within the framework of a classical chiral magnet Hamiltonian [7,8], which consists of competing Heisenberg exchange and Dzyaloshinskii-Moriya interactions [9,10] (DMIs). Recently, however, the quantum properties of skyrmions have garnered significant attention [11–26], particularly within the context of quantum spin Hamiltonians, due to their potential use as qubits in quantum computation [3,4,6], as carriers of topological bound modes [27,28], or as catalysts for topological superconductivity [29,30].

Unlike their classical counterparts, quantum skyrmions are quasiparticles that exhibit novel physical phenomena arising from the entanglement properties of the underlying spin system, usually spin-1/2 particles. In this work, we investigate quantum skyrmions in materials characterized by highly anisotropic DMI along a single spatial dimension while the Heisenberg exchange interaction remains isotropic. These materials, known as monoaxial chiral magnets [31], are of particular interest due to their unique ability to stabilize both skyrmion and antiskyrmion states with equal energy [32], in contrast to isotropic chiral magnets, where the antiskyrmion [33,34] always represents a higher energy state. Compounds such as $CrNb_3S_6$ [31,35–37], $MnNb_3S_6$ [38,39], and $CrTa_3S_6$ [40] are examples of materials that can be attributed to the class of monoaxial chiral magnets. The system $CrNb_3S_6$ has also been studied theoretically with density-functional theory calculations, which demonstrate negligible DMI presence in two out of three spatial directions [41,42]. In previous works studying monoaxial chiral magnets, an effective 1D Hamiltonian is assumed, which is fully capable of describing observable 1D spin-spiral (or soliton lattice) states. However, recent experimental work (Ref. [40]) demonstrates the existence of skyrmions in these materials, which requires considering at least a 2D Hamiltonian for theoretical modeling [32].

From a quantum perspective, skyrmions and antiskyrmions in monoaxial chiral magnets can thus form a many-body superposition state, dubbed the Schrödinger cat state, which cannot be described by classical micromagnetic models. It is worth noting that the term Schrödinger's cat, concerning a magnetic skyrmion in narrow racetrack devices, was recently introduced by Chudnovsky and Garanin in Ref. [6]. We want to stress that, in the present work, we utilize this name for the skyrmion-antiskyrmion superposition. The state of the system can be described by a wave function $|\psi\rangle$, which we use to calculate the magnetization vector field as an expectation value $\boldsymbol{m} = \langle\psi|\hat{\boldsymbol{S}}|\psi\rangle/\hbar$ of the spin operators $\hat{\boldsymbol{S}}$. In a classical case, the magnetization has a fixed length $|\boldsymbol{m}| = \text{const}$, while in the quantum case, it can deviate and even completely vanish.

In this work, we present our findings on the quantum properties of monoaxial skyrmions and antiskyrmions, and we provide a pathway toward their experimental observation through polarized neutron scattering. Furthermore, by solving the corresponding Schrödinger equation, we investigate the dynamics of a skyrmion-antiskyrmion superposition state in an external magnetic gradient field. By analyzing these dynamics in detail, we compare our results with predictions from simulations based on the classical Landau-Lifshitz and Thiele equations, thereby establishing a connection between the quantum Heisenberg model and micromagnetic theory in monoaxial chiral magnet systems.

The paper is structured as follows: In Sec. II, we introduce the quantum spin model used to describe monoaxial chiral magnets and we discuss its classical counterpart, including the phase diagram. Section III contains the main results of our paper, covering both static and dynamic properties of quantum skyrmions, antiskyrmions, and their superpositions,

[*]Contact author: stefan.liscak@uni.lu
[†]These authors contributed equally to this work.

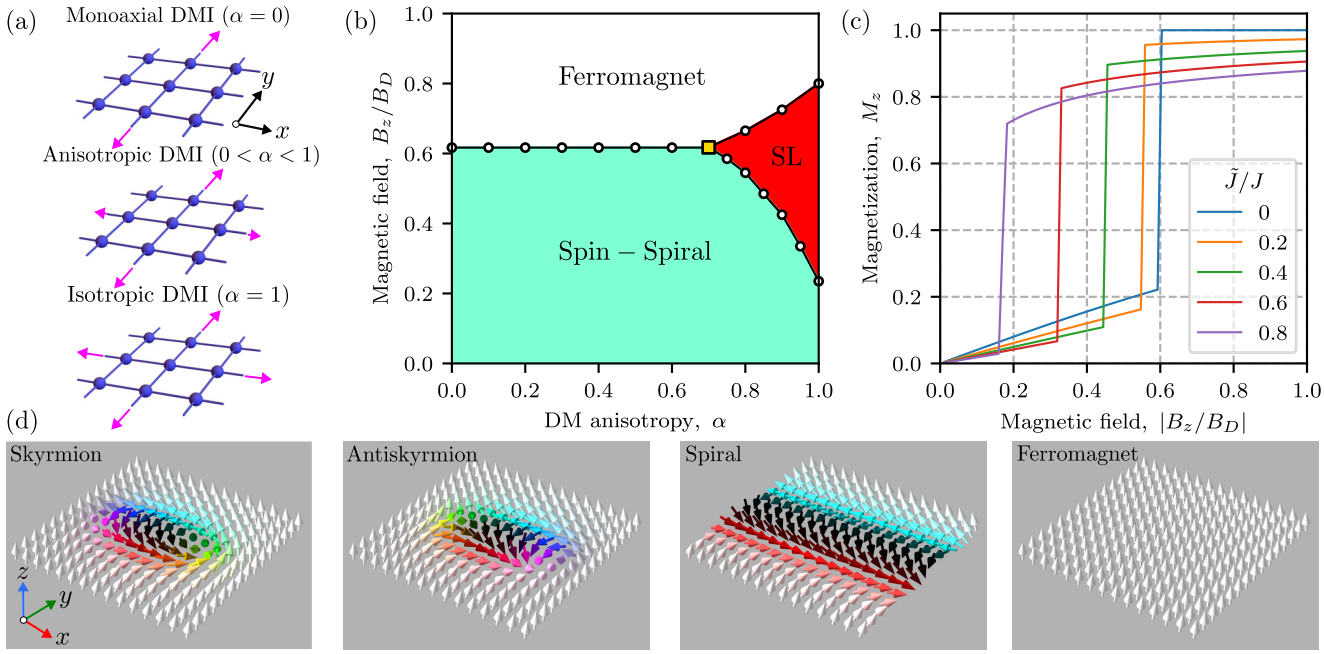

FIG. 1. (a) Different types of Bloch-like DMI: isotropic, anisotropic, and monoaxial, which can be distinguished by the parameter α in Eq. (2) in the main text. (b) Phase diagram in terms of α and the external field B_z/B_D, containing three phases: saturated ferromagnetic, spin-spiral, and skyrmion lattice (SL) states. (c) Transitions between spin-spiral and FM states for different values of magnetic field and easy-plane anisotropies $\tilde{J}$. (d) Magnetization textures relevant to the phase landscape in the monoaxial magnet, namely, the (anti)skyrmion, spin spiral, and ferromagnet. The arrow orientations are color coded based on the azimuthal and polar angles. White (black) arrows associate with spins pointing up (down) with respect to the plane.

organized into several focused subsections. Section IV provides a discussion about the potential nucleation mechanisms of skyrmion-antiskyrmion superpositions and their stability. Finally, Sec. V concludes the paper by summarizing the main findings of this study. Technical details and extended derivations are provided in Appendixes A–E.

II. MODEL AND METHODS

We consider the following Heisenberg Hamiltonian:

$$s\hat{H} = -\frac{1}{2}\sum_{\langle ij\rangle}[J\hat{\boldsymbol{S}}_i \cdot \hat{\boldsymbol{S}}_j + \boldsymbol{D}_{ij} \cdot (\hat{\boldsymbol{S}}_i \times \hat{\boldsymbol{S}}_j)] - \sum_i \boldsymbol{B}_i \cdot \hat{\boldsymbol{S}}_i, \quad (1)$$

where $\hat{\boldsymbol{S}}_i$ denotes the vector of spin operators for the spin at position $\boldsymbol{r}_i$, $\boldsymbol{B}_i = (B + 2B_{\text{grad}} y_i/(N_y - 1))\boldsymbol{e}_z$ is the sum of a uniform and a gradient Zeeman field, and N_y is the number of sites along y. First, we investigate the static properties for $B_{\text{grad}} = 0$. From now on, we consider the special case $s = 1/2$ and $J > 0$ (ferromagnetic exchange coupling). In the monoaxial limit, the DMI vector $\boldsymbol{D}_{ij} = D r_{ij}^y \boldsymbol{e}_y$ ($D > 0$ is the DMI amplitude) is given by the projection of $\boldsymbol{r}_{ij} = (r_{ij}^x, r_{ij}^y)$, the unit displacement vector between sites i and j, onto the y axis. For some calculations, we will consider a more general anisotropic DMI with anisotropy parameter α, so in the most general case we will use $\boldsymbol{D}_{ij} = D(\alpha r_{ij}^x \boldsymbol{e}_x + r_{ij}^y \boldsymbol{e}_y)$ [see Fig. 1(a)]. The DMI term then reads:

$$\begin{aligned}\boldsymbol{D}_{ij} \cdot (\hat{\boldsymbol{S}}_i \times \hat{\boldsymbol{S}}_j) = {} & D\alpha r_{ij}^x (\hat{S}_{i,y}\hat{S}_{j,z} - \hat{S}_{i,z}\hat{S}_{j,y}) \\ & + D r_{ij}^y (\hat{S}_{i,z}\hat{S}_{j,x} - \hat{S}_{i,x}\hat{S}_{j,z}). \end{aligned} \quad (2)$$

The parameter $\alpha \in [-1, 1]$ allows us to describe DMIs of various types: Bloch or bulk type favoring skyrmions ($\alpha > 0$), with the D_4 limit $\alpha = 1$, and antiskyrmions ($\alpha < 0$) with the D_{2d} limit $\alpha = -1$ [43].

Figure 1(b) contains the phase diagram in the atomistic spin model— the classical analog of Eq. (1)—for various DMI anisotropies in the micromagnetic limit. For these simulations, we optimized various magnetic phases with the conjugate gradient method for several external magnetic fields in units of $B_D = D^2/2J$ and dimensionless DMI anisotropy α. An interesting feature of the isotropic chiral magnets is their ability to host skyrmion lattices at a certain range of externally applied fields. In contrast, for monoaxial magnets, only two phases are possible: The ferromagnetic (FM) state and the spin-spiral state. For intermediate values of the DMI anisotropy ($\alpha \simeq 0.7$), there is a triple point in which the energies of the FM, the spin-spiral, and the skyrmion lattice phases coincide. In the range $0 \leqslant \alpha \lesssim 0.7$, magnetic skyrmions represent excited states.

Strictly speaking, monoaxial chiral magnets are characterized by the presence of effective easy-plane anisotropy. To model such anisotropy in the quantum system described by Eq. (1), we consider an additional term $\tilde{J}(\hat{S}_{i,x}\hat{S}_{j,x} + \hat{S}_{i,z}\hat{S}_{j,z})$ with coupling constant $\tilde{J} < 0$. Figure 1(c) shows the influence of magnetocrystalline anisotropy $\tilde{J}$ on the transition between FM and spin-spiral states in the monoaxial case, computed for the ground states of Eq. (1). From a symmetry point of view, to study the ground state of a monoaxial chiral magnet, it is enough to consider a one-dimensional chain along the y axis. Numerically, the Hamiltonian can be solved by exact diagonalization for small systems. We assume periodic

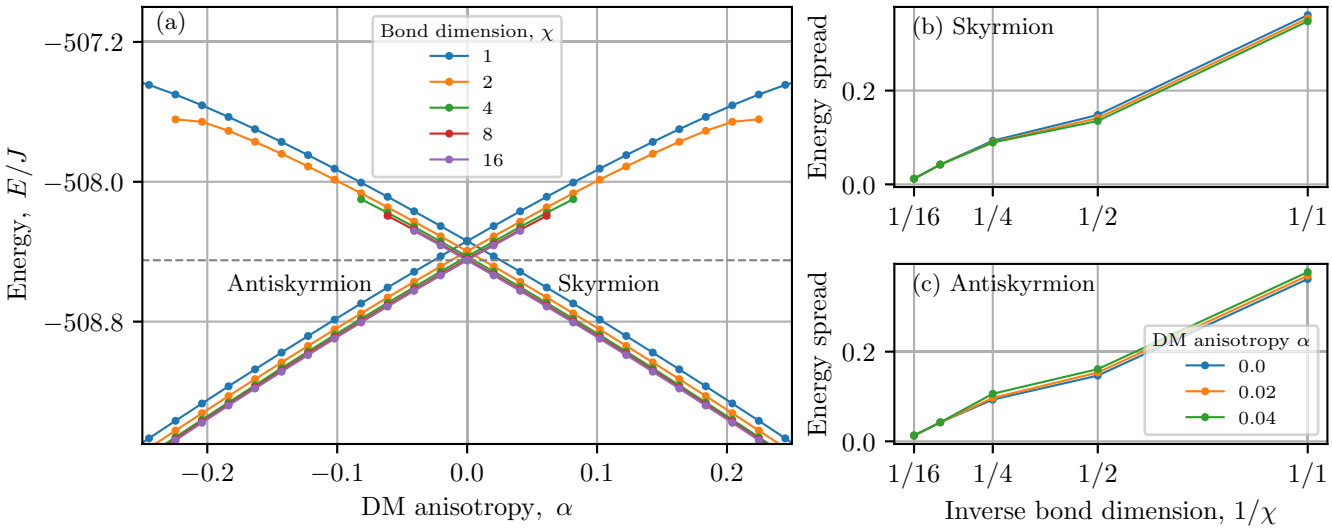

FIG. 2. (a) Energies of skyrmion and antiskyrmion eigenstates as functions of the parameter α at $B_{\text{grad}} = 0$ for different bond dimensions χ. Note that lines of excited states are getting shorter with increasing alpha, since the antiskyrmion (skyrmion) constitutes an eigenstate of $\hat{H}$ only in a region $\alpha \leqslant \alpha_c$ ($\alpha \geqslant -\alpha_c$). Using a linear extrapolation of the critical $\alpha_c(1/\chi)$, we find $\alpha_c = 0.03 \pm 0.02$ as $\chi \to \infty$. Complex conjugation ($\hat{K}$) maps between skyrmion and antiskyrmion states, which leads to a crossing of the spectral lines and a degeneracy at $\alpha = 0$. (b), (c) Energy spread $\langle(\hat{H} - E)^2\rangle / J^2$ at $\alpha = \{0, 0.02, 0.04\}$ versus the inverse bond dimension $1/\chi$ for skyrmions and antiskyrmions, respectively.

boundary conditions to eliminate boundary effects like the chiral surface twist. At low magnetic fields, the ground state is a spin spiral, while at stronger fields the ferromagnetic state is the lowest-energy state. The transition field depends on the anisotropy $\tilde{J}$ and gradually decreases for higher values of $\tilde{J}$. Thus, a nonzero anisotropy $\tilde{J} \neq 0$ only influences the value of the critical magnetic field, and in the following we omit it for simplicity and set $\tilde{J} = 0$.

Likewise, we neglect long-range dipolar field interactions in Eq. (1), as their inclusion leads only to quantitative changes in the results presented below. In the classical case, dipolar fields break the degeneracy between skyrmion and antiskyrmion states, but this effect can always be compensated for by a proper choice of DMI anisotropy α. Using Mumax3, we performed micromagnetic simulations for 2D skyrmions and antiskyrmions, accounting for dipole fields and different DMI anisotropies α. As shown in Appendix A, the skyrmion-antiskyrmion degeneracy point shifts toward a negative value of $\alpha = \alpha^* < 0$. For the particular choice of parameters, we can estimate $\alpha^* \simeq -0.022$. We expect this situation to be generic for various materials and sample thicknesses, which will change only quantitatively the degeneracy point α^*. The importance resides in the negative sign of α^*, which means that by controlling the sample thickness, for instance, one effectively modifies the dipolar-field contributions, and as a result, the exact value of the degeneracy point. Thus, one can think of α as an effective theoretical parameter that helps us analyze the system's properties at and near the degeneracy point for different types of chiral magnets: isotropic, anisotropic, and monoaxial ones.

It is worth pointing out that even though α represents a fine-tuned intrinsic parameter, it is possible to achieve some degree of experimental control by applying mechanical stress [44]. As a consequence, the results presented here for monoaxial chiral magnets will also hold for anisotropic DMI materials with $\alpha < 0$. Magnetic multilayers with surface-induced DMI due to strong spin-orbit coupling [45] can serve as an alternative physical system to study skyrmions. Manipulation of heavy-metal adatoms can effectively tune the DMI anisotropy [46], enabling the formation of monoaxial Néel-type skyrmions rather than monoaxial Bloch-type skyrmions. At the same time, we can expect to preserve all quantum effects discussed below. This follows from a global rotation of spins $\hat{\boldsymbol{S}} \to U\hat{\boldsymbol{S}}U^\dagger = R_z^T(\beta)\hat{\boldsymbol{S}}$ that leaves the exchange and Zeeman terms unchanged for any arbitrary angle β, while the DMI vectors are rotated accordingly, linking Bloch- and Néel-type DMI and the corresponding skyrmion textures. Thus, Néel and Bloch-type skyrmions represent the same texture viewed in different spin frames, being equivalent up to a uniform rotation in spin space.

We consider a two-dimensional simple cubic lattice and a rectangular domain of 31×15 sites, motivated by the elongated shape of the skyrmion and antiskyrmion. It has been established that ground state properties of similar ordered magnetic materials can be reliably calculated via DMRG [15,25,47–49]. In this work, we find that excited states are well approximated by the DMRG-X algorithm [50] [see Figs. 2(b) and 2(c)]. We fix $J = 1$ and $D = 0.5$ so the chosen system size is compatible with approximately one period of the spiral, given by $2\pi J/D \sim 13$ in units of the interatomic distance and to accommodate single-skyrmion excitations. In the case of the classical monoaxial chiral magnet ($\alpha = 0$), the low-energy excitations are the saturated state, as well as spin-spiral, skyrmion, and antiskyrmion states. While the first two can be ground states, depending on the value of the uniform Zeeman field, the last two are always excited states. To observe these states without additional surface twists on the system boundaries, we add boundary conditions in the form of classical environment spins, i.e., a single layer of

classical spins around the simulation domain pinned along the z axis [16,48]. Quantum spins interact with the classical environment through pairwise exchange and DM interactions similarly to Eq. (1), but where one spin operator is replaced by the pinned classical spin. Therefore, the interaction with the classical environment is effectively an additional Zeeman interaction for the boundary quantum spins. It is worth noting that, while in classical simulations we normally assume periodic boundary conditions to eliminate the surface twist effect, in the case of quantum simulations, fixed boundary conditions are preferable. The primary reason is the DMRG method we use for quantum simulations, which is generally less efficient for periodic systems. At the same time, from a physical point of view, as long as the system is large enough, we do not expect significant differences between fixed and periodic boundary conditions, and we select the former for technical reasons.

III. RESULTS

A. Quantum skyrmions and antiskyrmions

Skyrmion states can be found as excitations above the saturated state, for which we choose $B = 0.6B_{\mathrm{D}}$. Excitations can be simulated via the DMRG-X method [50], which targets energy eigenstates that maximize fidelity to an initial state. To target quantum (anti)skyrmion states, we start from classical (anti)skyrmion product states, more closely inspected in Sec. III B. The standard DMRG-X algorithm scales with the bond dimension χ as χ^6, and is therefore much more demanding than the standard DMRG algorithm used to approximate ground states, which instead scales with χ^3 [51]. The energy spread $\langle(\hat{H} - E)^2\rangle$, evaluated for the converged DMRG-X states, signals that the quality of the approximation depends on the bond dimension χ [see Figs. 2(b) and 2(c)] and reaches sufficient precision for $\chi_{\max} = 16$.

Skyrmion (antiskyrmion) states are numerically accessible for $\alpha > 0$ ($\alpha < 0$), but convergence to antiskyrmion (skyrmion) excitations is found only in a narrow window near zero. In the case $0 < \alpha \leqslant 1$, the skyrmion state $|\psi_{\mathrm{sk}}\rangle$ always has a lower energy than the antiskyrmion state $|\psi_{\mathrm{ask}}\rangle$ and vice versa for $-1 \leqslant \alpha < 0$ [see Fig. 2(a)]. This necessarily leads to a level crossing of the two states at $\alpha = 0$, where the energies of the skyrmion and antiskyrmion states are equal. The existence of a crossing can also be understood from the following symmetry arguments. Consider the complex conjugation operator $\hat{K}$. Due to the property $\hat{K}\hat{S}_y\hat{K} = -\hat{S}_y$, it follows from Eq. (2) that the Hamiltonian $\hat{H}(\alpha)$ satisfies $\hat{K}\hat{H}(\alpha)\hat{K} = \hat{H}(-\alpha)$. Therefore, the antiunitary operator $\hat{K}$ effectively inverts the sign of α in the Hamiltonian and maps the skyrmion eigenstates for α to antiskyrmion eigenstates for $-\alpha$. At $\alpha = 0$, the Hamiltonian is real; therefore, it commutes with $\hat{K}$, which protects a twofold degeneracy. The general state is an arbitrary superposition, i.e.,

$$|\psi\rangle = c\hat{K}\,|\psi_{\mathrm{sk}}\rangle + \sqrt{1-c^2}\mathrm{e}^{\mathrm{i}\varphi}\,|\psi_{\mathrm{sk}}\rangle\,. \tag{3}$$

Spin expectation values of the symmetric superposition, $c = 1/\sqrt{2}$, are shown in Fig. 3(b).

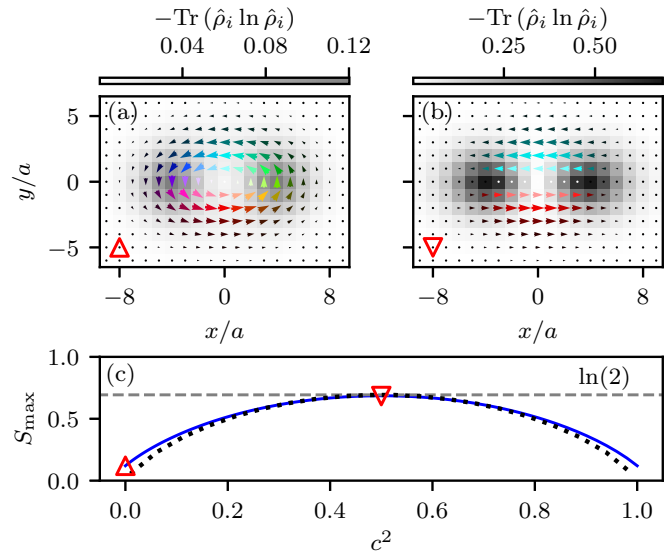

FIG. 3. Local von Neumann entanglement entropy presented as a grayscale background for the skyrmion state (a) and the symmetric superposition (b). The colored arrows represent the expectation values of local magnetization. (c) Maximum of the local von Neumann entropy for arbitrary superpositions. The computed $S_{\max}$ from MPS simulations (blue line) agrees very well with the analytic estimate in Eq. (10) (black dots). Note that due to the hermiticity of $\hat{\rho}_i$, its eigenvalues are invariant under complex conjugation, thus yielding the same entanglement entropy for both skyrmion and antiskyrmion states.

Since $\hat{K}\sigma_y\hat{K} = -\sigma_y$ (and σ_x, σ_z are invariant), the conjugated state $\hat{K}\,|\psi_{\mathrm{sk}}\rangle$ has a magnetic texture in the spin expectation values that carries the negative topological charge of $|\psi_{\mathrm{sk}}\rangle$. This justifies calling $|\psi_{\mathrm{ask}}\rangle = \hat{K}\,|\psi_{\mathrm{sk}}\rangle$ the corresponding antiskyrmion state. Note that the skyrmion and conjugate skyrmion states are simultaneously eigenstates only at the $\hat{K}$-symmetric point $\alpha = 0$.

B. Product state approximation and entanglement

In our work, we utilize product states either as initial states for the DMRG(-X) routines or as reference states to estimate the quantumness of the eigenstates. We represent these states as products of spin-1/2 states with predetermined projections of the magnetic moment:

$$\begin{aligned}|\phi_{\mathrm{sk}}\rangle &= \prod_i |\boldsymbol{n}_i\rangle = \prod_i e^{-\mathrm{i}\Phi_i\hat{S}_i^z} e^{-\mathrm{i}\Theta_i\hat{S}_i^y}\,|\Uparrow\rangle\,,\\ &= \prod_i (e^{-\mathrm{i}\Phi_i/2}\cos\Theta_i/2,\, e^{\mathrm{i}\Phi_i/2}\sin\Theta_i/2)^T\,.\end{aligned} \tag{4}$$

This construction ensures that each local spinor $|\boldsymbol{n}_i\rangle$ is aligned with the magnetic moment $\frac{1}{2}\boldsymbol{n}_i = \langle\boldsymbol{n}_i|\,\hat{\boldsymbol{S}}_i\,|\boldsymbol{n}_i\rangle = \frac{1}{2}(\sin\Theta_i\cos\Phi_i, \sin\Theta_i\sin\Phi_i, \cos\Theta_i)$. Note that the $\pi\mathbb{Z}$ phase after full revolutions does not contribute to the expectation value. We choose the initial state of the DMRG-X algorithm as a product state with an arbitrary magnetic texture by imposing the set of angles $\{\Theta_i, \Phi_i\}$. For our purposes, this typically corresponds to the skyrmion texture. In particular, we start from the product state $\prod_i |\boldsymbol{n}(\Theta_i, \Phi_i)\rangle$ (see Appendix B) with

the choice

$$\Theta_i = 2\arctan(\sinh(r_i/a)/\sinh(R/a)) - \pi,$$
$$\Phi_i = \mathrm{sign}(\alpha)[\phi(x_i, y_i) + \pi/2],$$
$$R = 3a, \tag{5}$$

and where ϕ denotes the azimuthal angle spanned by the x and y components of the spin.

Using bond dimension up to $\chi = 16$ and applying DMRG-X, we achieve convergence to approximate eigenstates of $\hat{H}$, while keeping the bond dimension fixed to $\chi = 1$ results in an energetically optimized product state.

For an antiskyrmion state, we have a product of complex-conjugated states:

$$|\phi_{\mathrm{ask}}\rangle = \prod_i \hat{K}\,|\boldsymbol{n}_i\rangle \equiv \prod_i |\overline{\boldsymbol{n}}_i\rangle\,, \tag{6}$$

where $\hat{K}$ is the complex conjugation operator. The associated expectation values are

$$\langle\phi_{\mathrm{ask}}|\hat{\boldsymbol{S}}_i|\phi_{\mathrm{ask}}\rangle = \langle\overline{\boldsymbol{n}}_i|\hat{\boldsymbol{S}}_i|\overline{\boldsymbol{n}}_i\rangle = \langle\boldsymbol{n}_i|\hat{\boldsymbol{S}}_i^*|\boldsymbol{n}_i\rangle = \tfrac{1}{2}\overline{\boldsymbol{n}}_i, \tag{7}$$

and it is straightforward to recognize that the magnetization profiles of the skyrmion and antiskyrmion product states are related via a sign exchange of the y component, $(\overline{n}_{i,x}, \overline{n}_{i,y}, \overline{n}_{i,z}) = (n_{i,x}, -n_{i,y}, n_{i,z})$.

While individual product states lack the key quantum features of a matrix product state (MPS) [52], such as entanglement, they can be used to predict the qualitative behavior of individual (anti)skyrmion states, thus serving as an adequate approximation in a handful of cases. Several measures may be introduced to quantify to which extent a semiclassical product state acceptably approximates an MPS. One such quantity is the local von Neumann entanglement entropy. To calculate the von Neumann entropy at site i, we construct the reduced density matrix,

$$\hat{\rho}_i = \mathrm{Tr}_{\bar{i}}\,|\psi\rangle\langle\psi|\,, \tag{8}$$

where $\mathrm{Tr}_{\bar{i}}$ denotes a partial trace over the entire complement of i and $|\psi\rangle$ represents the MPS. The entropy is then defined as

$$S_i = -\mathrm{Tr}(\hat{\rho}_i \ln \hat{\rho}_i). \tag{9}$$

If the site i is completely disentangled from its environment, as is the case for product states, its reduced matrix becomes a projector with eigenvalues $\{0, 1\}$, leading to vanishing entropy. In Fig. 3, we present the von Neumann entropy calculated for different matrix product states with bond dimension $\chi = 16$. We observe that quantum effects play a subleading role for individual (anti)skyrmion states. This manifests in relatively low local entanglement compared to the maximal value ($\ln 2$ for spin-1/2). Thus, we conclude that the product states with sharp local magnetization are an adequate candidate to approximate the (anti)skyrmion MPS states. In contrast, the entanglement increases steeply at two regions of noncollinearity of the superposition state in Fig. 3(c), which signals large deviations from a product state. Within these regions, the expected local magnetization also tends to zero. These features can be explained by a coherent superposition of skyrmion-antiskyrmion product states, i.e., by the approximation $|\psi\rangle \approx c\,|\phi_{\mathrm{ask}}\rangle + \sqrt{1-c^2}e^{i\varphi}\,|\phi_{\mathrm{sk}}\rangle$.

At sites i', where $\langle\phi_{\mathrm{ask}}|\hat{S}_{i',z}|\phi_{\mathrm{ask}}\rangle = 1/2$, the reduced density matrix is given by $\hat{\rho}_{i'} = |\uparrow\rangle\langle\uparrow|$, leading to vanishing entanglement. In contrast, due to the conjugate nature of the (anti)skyrmion states, at sites where the y component of the spin expectation value reaches its maximum value, we find $\hat{\rho}_{\max} \approx c^2\,|+\rangle\langle+| + (1-c^2)\,|-\rangle\langle-|$, where $|\pm\rangle$ denote the eigenstates of the spin operator along the y direction (we neglect vanishingly small overlap elements, which we discuss in more detail in Sec. III C). This allows us to estimate the entropy in the superposition as

$$S_{\max} \approx -c^2 \ln c^2 - (1-c^2)\ln(1-c^2), \tag{10}$$

which is in very good agreement with the simulated results presented in Fig. 3(c).

It is straightforward to evaluate the spin polarization at these points for generic superpositions, i.e., $n_y = 2\mathrm{Tr}\hat{S}_{\max,y}\hat{\rho}_{\max} \approx 2c^2 - 1$, such that we establish a connection between entanglement entropy and average magnetization:

$$S_{\max} \approx \frac{1}{2}\left(\ln 4 - \ln\left(1-n_y^2\right) - n_y \ln\left(\frac{1+n_y}{1-n_y}\right)\right). \tag{11}$$

In conclusion, for symmetric superpositions $c^2 = 1/2$, the local magnetization is strongly suppressed, and spins located at these special points are maximally entangled with the environment [see Fig. 3(b)]. Physically, the $c = 1/\sqrt{2}$ superposition states are the magnetic analogs of Schrödinger cat states. Under the influence of a magnetic field gradient, the skyrmion and antiskyrmion states have a different time evolution as predicted by Thiele's equation [53] applied to our particular setup; see Appendix D. For the superposition state, this leads to a spatial separation of the skyrmion and antiskyrmion wave functions over time, which we will discuss further below (see Fig. 5).

C. Orthogonality centers

The previous section concerned the appearance of two regions with reduced magnetization length and increased entanglement for $0 < c < 1$. In the product state approximation, it can be shown that the centers of these regions are tied to the orthogonality between the magnetization profiles of skyrmion and antiskyrmion. The mutual overlap of the states $|\phi_{\mathrm{sk}}\rangle$ and $|\phi_{\mathrm{ask}}\rangle$ can be decomposed into a product of local overlaps for each individual node,

$$\langle\phi_{\mathrm{sk}}|\phi_{\mathrm{ask}}\rangle = \prod_i \langle\boldsymbol{n}_i|\overline{\boldsymbol{n}}_i\rangle \equiv \prod_i v_i$$
$$= \prod_i (\cos\Phi_i + i\sin\Phi_i\cos\Theta_i), \tag{12}$$

where the parametrization $|\boldsymbol{n}_i\rangle = |\boldsymbol{n}(\Theta_i, \Phi_i)\rangle$ from Eq. (4) is used. With the local magnetization vectors $\frac{1}{2}\boldsymbol{n}(\Theta_i, \Phi_i) = \frac{1}{2}(\sin\Theta_i\cos\Phi_i, \sin\Theta_i\sin\Phi_i, \cos\Theta_i)$, one obtains a phase-gauge independent expression:

$$|v_i|^2 = (1-n_{i,y})(1+n_{i,y}). \tag{13}$$

Therefore, at sites i where the y component of spin expectation values reaches ± 1, the overlap elements v_i vanish. As long as this condition is met anywhere, the inner product (12) is

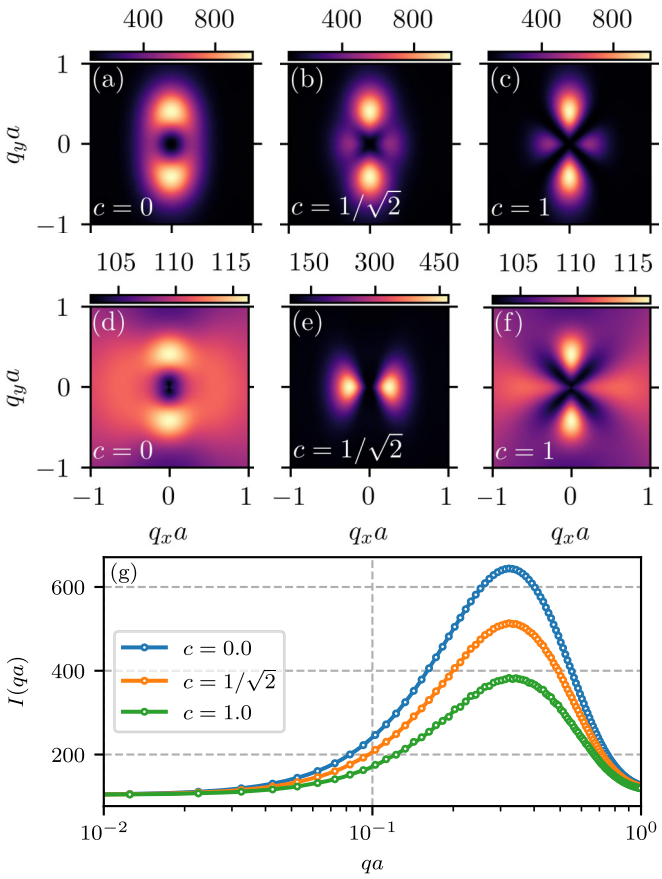

FIG. 4. (a)–(c) Spin-flip SANS cross sections $d\Sigma_{\rm sf}/d\Omega$ in arbitrary units for skyrmion state ($c = 0$), symmetric superposition ($c = 1/\sqrt{2}$), and antiskyrmion state ($c = 1$). (d)–(f) Their connected parts. Note the change of scale in (e) compared to (d) and (f). The signature of the superposition state manifests in two pronounced peaks along q_x. (g) Azimuthally averaged spin-flip SANS intensity [of the data from (a)–(c)] as a function of qa (log-linear scale).

dominated by a zero overlap and vanishes as well. For this reason, we call these special points orthogonality centers.

Due to the spatial separation of the orthogonality centers, energy-degenerate skyrmions and antiskyrmions couple only weakly via local interactions. This can be recognized in the matrix elements of the spin operator, which are strongly suppressed by the product of local overlap elements v_i, i.e.,

$$\langle\psi_{\rm sk}|\hat{\boldsymbol{S}}_i|\psi_{\rm ask}\rangle = \langle \boldsymbol{n}_i|\hat{\boldsymbol{S}}_i|\overline{\boldsymbol{n}}_i\rangle \prod_{j\neq i} v_j,$$

$$\langle \boldsymbol{n}_i|\hat{\boldsymbol{S}}_i|\overline{\boldsymbol{n}}_i\rangle = \frac{1}{2}\begin{pmatrix} \sin\Theta_i \\ 0 \\ \cos\Theta_i\cos\Phi_i + \mathrm{i}\sin\Phi_i \end{pmatrix}. \tag{14}$$

Note that in Eqs. (12) and (14), the last equations are phase-gauge dependent. Since the matrix element in Eqs. (14) is strongly suppressed by the product of overlap elements v_j, local perturbations only weakly couple the two states. A small yet finite coupling induced by a local perturbation of an orthogonality center can persist due to lattice effects: The local orthogonality can be imperfect, since the centers might not necessarily satisfy $\boldsymbol{n} = \pm\boldsymbol{e}_y$. Crucially, such imperfection persists regardless of the overall system size and diminishes when the lattice spacing becomes much smaller than the characteristic skyrmion size. Thus, we expect a certain robustness of (anti-)skyrmion states against (sums of) local perturbations. Although these perturbations may induce collective motion (see Sec. III E), they are unlikely candidates for the development of protocols to nucleate superposition states. We discuss potential strategies for the nucleation and manipulation of superposition states in a dedicated section (see Sec. IV).

D. Magnetic SANS as a probe of skyrmionic Schrödinger cat states

The properties of the skyrmion state $|\psi\rangle$ may be probed using the magnetic small-angle neutron scattering (SANS) technique (see, e.g., Refs. [54,55] for reviews). This method is a key experimental tool, since it offers, quite uniquely, the possibility to investigate the magnetic microstructure in the volume of magnetic media and on the relevant length scales (∼1–1000 nm). The scattering contrast for magnetic SANS is related to spatial nanometer-scale variations in the magnitude and orientation of the magnetization texture. Here, we calculate a set of SANS observables for the elastic scattering of a neutron beam polarized parallel to the field $\boldsymbol{B} = B\boldsymbol{e}_z$ with a primary focus on the so-called spin-flip SANS cross section. The latter quantity can be measured using uniaxial polarization analysis and is given by

$$\frac{d\Sigma_{\rm sf}}{d\Omega} \propto \sum_{\alpha,\beta=x,y}\left(\delta_{\alpha\beta} - \frac{q_\alpha q_\beta}{q^2}\right)\mathcal{S}_{\alpha\beta}(\boldsymbol{q}), \tag{15}$$

where $\boldsymbol{q} = (q_x, q_y, q_z)$ is the momentum transfer vector and $\mathcal{S}_{\alpha\beta}(\boldsymbol{q})$ are the structure factors

$$\mathcal{S}_{\alpha\beta}(\boldsymbol{q}) = \sum_{ij} e^{-i\boldsymbol{q}\cdot(\boldsymbol{r}_i-\boldsymbol{r}_j)}\,\langle\psi|\hat{S}_{i,\alpha}\hat{S}_{j,\beta}|\psi\rangle\,. \tag{16}$$

The unpolarized magnetic SANS cross section $d\Sigma/d\Omega$ is similar to Eq. (15), but the sum is taken over all components $\{x, y, z\}$ of the structure factors. In the small-angle regime, the component of $\boldsymbol{q}$ along the incident beam is significantly smaller than the other two components, i.e., $q_z \approx 0$. This implies that the only difference between the spin-flip and the unpolarized SANS cross section is a single structure factor, $d\Sigma/d\Omega - d\Sigma_{\rm sf}/d\Omega = \mathcal{S}_{zz}$. In the product state approximation (see Secs. III B and III C), $\mathcal{S}_{zz}$ forms a common background for skyrmions and antiskyrmions. The background variation is largely suppressed for $0 < c < 1$ due to the opposite local order between the skyrmion and antiskyrmion states that contribute to the superposition. For this reason, $\mathcal{S}_{zz}$ effectively represents the same shift for all amplitudes c, so individual superpositions could also be detected in unpolarized SANS experiments.

In Figs. 4(a)–4(c), we display the spin-flip SANS cross section for different superpositions. The equal-part superposition bears qualitative aspects of both the skyrmion and antiskyrmion cross sections, i.e., $d\Sigma_{\rm sf}/d\Omega \approx c^2 d\Sigma_{\rm sf}^{\rm ask}/d\Omega + (1-c^2)d\Sigma_{\rm sf}^{\rm sk}/d\Omega$. This can also be observed in the spin-flip intensity $I_{\rm sf}(q)$ obtained by averaging out the azimuthal degree

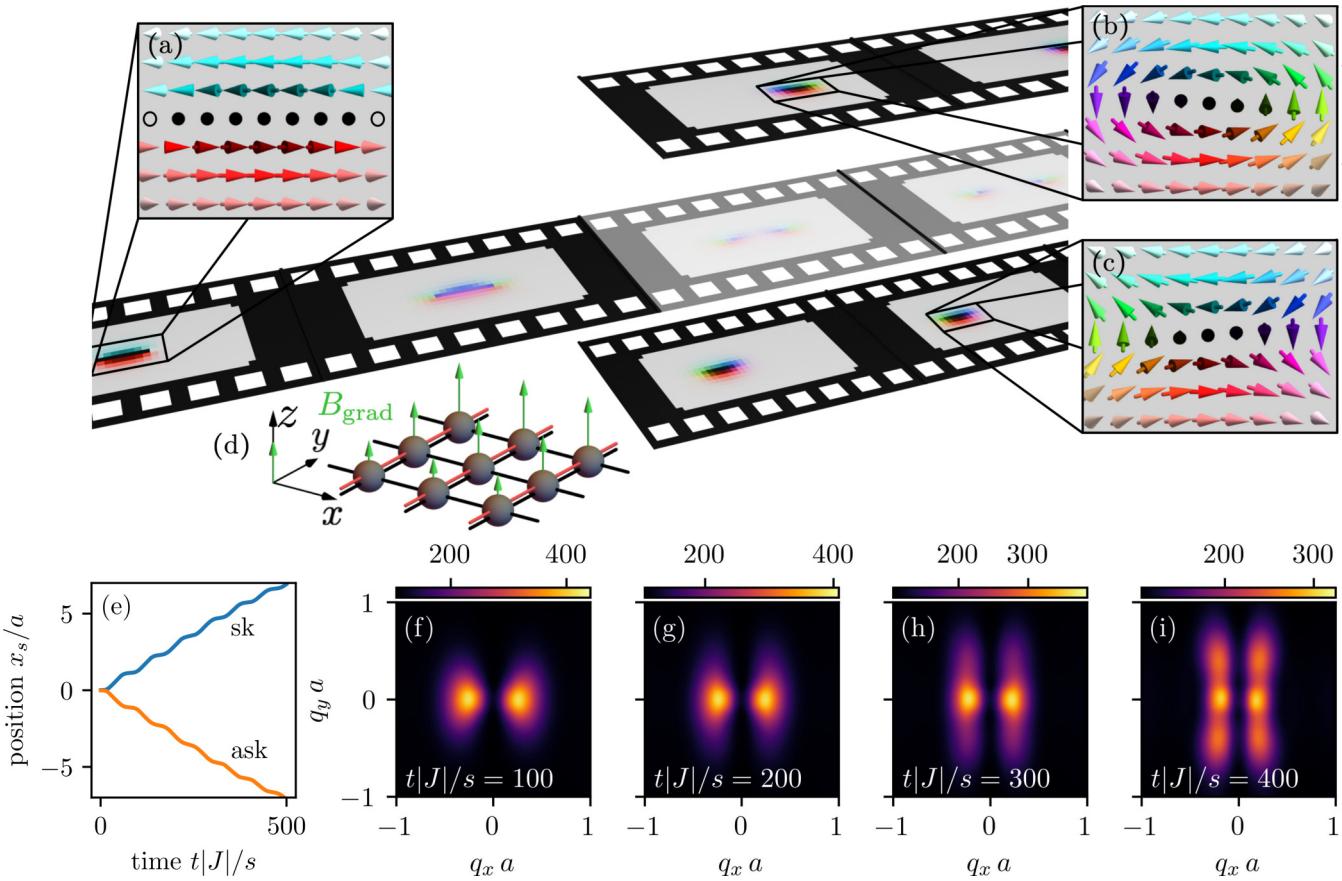

FIG. 5. The gradient-field-induced time evolution of the Schrödinger cat state shown in (a), which is an equal superposition of a symmetric skyrmion (b) and antiskyrmion (c). A projective measurement made after the second snapshot (illustrated by transparency) leads to the collapse of the wave function, and, as a result, the system evolves as a classical skyrmion or antiskyrmion. (d) Sketch of the square lattice, where the nodes represent spin-1/2 sites. Black and red bonds correspond to exchange and Dzyaloshinskii-Moriya interactions, respectively, and green arrows show the Zeeman field perturbation. (e) Change of the average position for (anti)skyrmions under the field $B_{\text{grad}}/J = -0.02$. (f)–(i) Connected part of the spin-flip SANS cross section at times $t|J|/s \in \{100, 200, 300, 400\}$, calculated for the symmetric superposition state.

of freedom in the q_x-q_y plane:

$$I_{\text{sf}}(q) = \frac{1}{2\pi}\int_0^{2\pi} \frac{d\Sigma_{\text{sf}}}{d\Omega}(q,\theta)d\theta. \tag{17}$$

The results for $I_{\text{sf}}(q)$ are displayed in Fig. 4(g), revealing that the signal of the symmetric superposition corresponds to the average between the skyrmion and antiskyrmion cases.

In contrast, the differences between semiclassical and superposition states are well pronounced in the *connected* part of the spin-flip SANS cross section $d\Sigma_{\text{sf}}^{\text{conn}}/d\Omega$, where in Eq. (16) we replace

$$\begin{aligned} \langle \hat{S}_{i,\alpha}\hat{S}_{j,\beta}\rangle &\to \langle\langle \hat{S}_{i,\alpha}\hat{S}_{j,\beta}\rangle\rangle, \\ \langle\langle \hat{S}_{i,\alpha}\hat{S}_{j,\beta}\rangle\rangle &= \langle \hat{S}_{i,\alpha}\hat{S}_{j,\beta}\rangle - \langle \hat{S}_{i,\alpha}\rangle\langle \hat{S}_{j,\beta}\rangle . \end{aligned} \tag{18}$$

We emphasize that, in contrast to the full correlator [Eq. (16)], the connected part of the spin-flip SANS cross section cannot be directly obtained in a SANS experiment. Its reconstruction additionally requires spatial resolution of the local magnetization profile, e.g., through magnetic force microscopy or spin-resolved scanning tunneling microscopy. Figures 4(d)–4(f) show that this theoretical quantity is ideally suited to detect the difference between states with high and zero site-to-site entanglement.

As we show in Sec. III B and Appendix B, (anti)skyrmion matrix product states, obtained from the DMRG-X algorithm, exhibit significant overlap with simple product state approximations. However, these product-state approximations yield no special structure in the connected cross sections. Therefore, the structure of the signal in Figs. 4(d) and 4(f) emerges exclusively from quantum effects. Note that the variations between the minima and maxima in Figs. 4(d) and 4(f) are approximately a factor 20 smaller compared to Fig. 4(e) for the chosen parameters. The pronounced double-peak structure can instead be attributed to the state superposition alone (see Appendix C, Fig. 8).

The results shown in Figs. 4(a)–4(c) and 4(g) reflect the elastic SANS signal, which typically provides the dominant scattering contribution in SANS experiments measuring an energy-integrated cross section. In addition to this elastic contribution, there exists a narrow window in the small-angle regime where inelastic magnon scattering may occur (see, e.g., Refs. [56,57]). The inelastic SANS signal may provide another avenue to detect superposition states. The extent of this inelastic regime is governed by the applied magnetic field, the intrinsic magnetic parameters of the material (such as anisotropy, magnetostatic interaction, and DMI) and, most importantly, the spin-wave dispersion relation. For the present

monoaxial DMI system, however, the dispersion relation has not yet been established, and its investigation lies beyond the scope of this work.

E. Dynamics under a magnetic field gradient

We consider the dynamics of (anti)skyrmion excitations under the influence of a magnetic field with a small gradient along the y direction. For this purpose, we numerically solve the Schrödinger equation $\mathrm{i}\partial_t |\psi\rangle = \hat{H} |\psi\rangle$ using the time-dependent variational principle (TDVP) [58,59] (see Appendix E for convergence results). The superposition state of Eq. (3) evolves according to

$$|\psi(t)\rangle = c\,|\psi_{\mathrm{ask}}(t)\rangle + \sqrt{1-c^2}\mathrm{e}^{\mathrm{i}\varphi}\,|\psi_{\mathrm{sk}}(t)\rangle\,. \tag{19}$$

Due to the $\hat{K}$-symmetry of $\hat{H}$ at $\alpha = 0$, the trajectories of the initial states are given by

$$|\psi_{\mathrm{sk}}(t)\rangle = \mathrm{e}^{-\mathrm{i}\hat{H}t}\,|\psi_{\mathrm{sk}}(0)\rangle\,, \tag{20}$$

$$|\psi_{\mathrm{ask}}(t)\rangle = \mathrm{e}^{-\mathrm{i}\hat{H}t}\hat{K}\,|\psi_{\mathrm{sk}}(0)\rangle = \hat{K}\,|\psi_{\mathrm{sk}}(-t)\rangle\,. \tag{21}$$

Therefore, skyrmions and antiskyrmions share a particle-antiparticle relationship: They have opposite topological charges, and their dynamics are related via time reversal.

To demonstrate a coherent motion of the wave, we compute spin expectation values at times t,

$$\boldsymbol{m}_{i,s}(t) = \langle\psi_s(t)|\hat{\boldsymbol{S}}_i|\psi_s(t)\rangle\,, \quad s \in \{\mathrm{sk}, \mathrm{ask}\}, \tag{22}$$

and analyze the evolution of the average skyrmion position, $(x_s(t), y_s(t)) = \sum_i \boldsymbol{r}_i m^z_{i,s}(t) / \sum_i m^z_{i,s}(t)$ (see Fig. 5). The skyrmion and antiskyrmion move with opposite Hall angles, which is compatible with the solutions of Thiele's classical equation for rigid skyrmion motion in the absence of dissipation, i.e., $\dot{x}_s \propto B_{\mathrm{grad}}/Q$, $\dot{y}_s = 0$, where $Q = \pm 1$ is the topological charge (see Appendix D). In Fig. 5(e), we display the change of the average position for (anti)skyrmions under the Zeeman field perturbations. At the perturbation amplitude $B_{\mathrm{grad}}/J = -0.02$, we find an average velocity of $v_s \approx 0.014|J|Qa$ via a linear fit of the trajectories. This presents an adequate match to the result $v_s \approx 0.0137|J|Qa$ obtained from the Thiele equation. Similarly to Sec. III B, we approximate $|\psi(t)\rangle \approx c\,|\phi_{\mathrm{ask}}(t)\rangle + \sqrt{1-c^2}\mathrm{e}^{\mathrm{i}\varphi}\,|\phi_{\mathrm{sk}}(t)\rangle$, and find

$$\langle\psi(t)|\hat{\boldsymbol{S}}_i|\psi(t)\rangle \approx c^2\boldsymbol{m}_{i,\mathrm{ask}}(t) + (1-c^2)\boldsymbol{m}_{i,\mathrm{sk}}(t), \tag{23}$$

where we again neglect small matrix elements $\langle\phi_{\mathrm{sk}}(t)|\hat{\boldsymbol{S}}_i|\phi_{\mathrm{ask}}(t)\rangle$. Note that the matrix elements become more suppressed over time as the skyrmion and antiskyrmion centers move in opposite directions.

In conclusion, we find that the spin expectation value equals the weighted average, which is further confirmed by the MPS simulations. This dynamics can be qualitatively described with the classical Landau-Lifshitz equation by simulating the (classical) skyrmion and antiskyrmion wavefront separately and then constructing the superposition state of interest according to Eq. (23). Due to subleading quantum effects in the individual wavefronts, the resulting deviation is minor (see the comparison in Fig. 10). In an experiment, the spin expectation value would result from projective measurements such that the superposition state collapses to either skyrmion or antiskyrmion states. Consequently, the hypothetical observer would measure $\boldsymbol{m}_{i,\mathrm{ask}}(t)$ or $\boldsymbol{m}_{i,\mathrm{sk}}(t)$ with probability c^2 or $1-c^2$, respectively.

To further characterize the wavefront behavior, we examine the connected part of the polarized SANS cross section at different times [see Figs. 5(f)–5(i)]. For the symmetric superposition state, we observe a broadening of the two central peaks along q_y, indicative of distinct wavefront dynamics in the symmetric superposition states. This behavior can be understood from two features of the structure factor components that we derive in Appendix C, i.e., an increasing signal $\propto \sin^2(\boldsymbol{q}\cdot\boldsymbol{v}t)\mathcal{F}_x(\boldsymbol{q})$ with four peaks around the origin, and a decreasing component $\propto \cos^2(\boldsymbol{q}\cdot\boldsymbol{v}t)\mathcal{F}_y(\boldsymbol{q})$ with two peaks around the origin. Tracking the temporal change of the overall amplitude of these peaks thus allows us to estimate the velocity of the wavefront.

IV. DISCUSSION

Spontaneous nucleation of magnetic skyrmions can be achieved by thermal fluctuations and laser excitations that were experimentally realized in thin films and bulk systems of chiral magnets [60–62]. Numerical simulations on smaller 2D and 3D systems [63–65] agree well with these experiments and even provide insight into how more sophisticated spin textures can be nucleated. Thus, we expect similar behavior with skyrmion and antiskyrmion nucleation also in a 2D system of monoaxial chiral magnets, similarly to the approach based on temperature-induced breaking of the spin-spiral state in a thin film of $CrNb_3S_6$, reported in Ref. [40]. It is worth noting that the energy landscape in these materials is much simpler compared to an isotropic chiral magnet, so the appearance of a smaller number of metastable states can be expected in experiments. Controllable nucleation of a skyrmion state with predefined properties typically requires a special experimental protocol that includes local modification of sample properties (e.g., anisotropy reduction) and the application of localized in-space and/or time excitation (e.g., laser or current pulses), as reported in Refs. [66–69].

Having a skyrmion (or antiskyrmion) state in the system, preparation of a superposition state represents a challenging problem both experimentally and theoretically. For the coupled skyrmion-antiskyrmion state representing a qubit state discussed in this work, there is no approach to prepare such a state with a classical micromagnetism framework due to topological reasons, i.e., skyrmion and antiskyrmion cannot continuously transform into each other. Therefore, we can deduce that the mechanisms to achieve such a state must rely on theories beyond classical magnetism. The most promising approach for us to prepare the superposition state seems to rely on the light-matter interaction recently discussed in Ref. [70]. According to this approach, one can shine a laser pulse onto the magnetic system with various momenta (p) and angular momenta (l) [71]. To study this in simulations, one has to account for the presence of the so-called Laguerre-Gauss beams [72,73], which can be modeled as an effective magnetic field pulse, $\delta\boldsymbol{B} = B_r\boldsymbol{e}_r + B_\phi\boldsymbol{e}_\phi$, where in-plane components B_r and B_ϕ are time- and space-dependent functions that contain information of p and l. As recently theoretically demonstrated [74], there is a one-to-one correspondence

between laser beam parameters and the topology of the skyrmion one can nucleate with this laser pulse. Thus, one can argue that a sequential laser pulse with different (p, l) applied to a skyrmion state could lead to modifying the state's topological charge and formation of the superposition state. An alternative approach, which might be possible in the presence of a coupling mechanism between the photon angular momentum and the skyrmion vorticity, is to shine a laser pulse prepared as a superposition of several (p, l) modes onto the polarized state. This could potentially represent a method toward a more direct formation of the cat state. It is worth pointing out that the quantum spin dynamics simulation of this process represents a challenge due to the absence of an efficient way to store such a state and perform numerical integration of the Schrödinger equation with sufficient accuracy, which can also stimulate further development of computational physics methods. It is furthermore noteworthy that the experimental realization of cat-state preparation poses a challenge, requiring advances in existing experimental techniques and improvements in theoretical modeling of quantum many-body states. The interplay between light and magnetism could be the key to overcome this challenge, however, the preparation route for the cat state remains an open question, which motivates further investigation.

In the simplest case, we reported that the degeneracy is protected by complex conjugation symmetry—a nonlocal transformation. By relying on product state approximations, we revealed that the (vanishing) skyrmion-antiskyrmion overlap elements are dominated by two orthogonality centers, such that local perturbations do not easily couple them. For ferromagnetic Heisenberg systems, it is well-known that magnetic states with different topological charges are energetically separated because transitions including a change of the topological charge also require the appearance of magnetic singularities. In the case of monoaxial DMI, states of topological charges with equal absolute magnitude are energy-degenerate, but those of different absolute magnitude are still energetically well separated. As a result, the energy-degenerate skyrmion-antiskyrmion superposition states are unlikely to decay into other states through quantum tunneling induced by weak local disturbances, and we conjecture decoherence times on the order of (anti)skyrmion lifetimes in the platform [3,75].

The monoaxial DMI limit studied here corresponds to a particular, symmetry-enhanced regime of the general chiral magnet Hamiltonian. We investigate this limit as a controlled and analytically transparent framework in which the degeneracy between skyrmion and antiskyrmion states follows directly from symmetry. The purpose of the present work is therefore not to provide material-specific predictions but to establish, within a minimal model, the existence and properties of a well-defined two-state manifold that supports skyrmion–antiskyrmion superpositions. Deviations from strict monoaxiality, e.g., finite DMI anisotropy or nonlocal dipolar interactions, explicitly break the discrete symmetry relating the two textures and introduce a finite energy splitting. In an effective two-level description, these terms act as weak bias fields, as they only shift the degeneracy point while leaving the conceptual framework of the construction intact (see Fig. 6). Finally, we would like to point out that the proposed minimal model is fundamentally limited for controlling cat states, motivating further extension. As skyrmion and antiskyrmion states are related by complex conjugation, we conjecture that nonlocal perturbations may be required to couple the two excitations. We believe that the effective interaction between magnetic moments and light could potentially mediate a suitable hybridization mechanism.

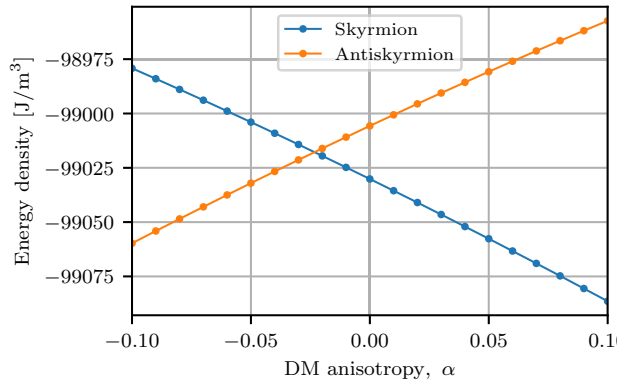

FIG. 6. Energies of skyrmion and antiskyrmion states as a function of the DM anisotropy parameter α, taking into account the presence of dipolar fields. The energy degeneracy point corresponds to $\alpha^* = -0.022$.

V. CONCLUSIONS

In this work, we studied the static and dynamic properties of quantum skyrmion and antiskyrmion excitations in monoaxial chiral magnets. Using symmetry arguments and density matrix renormalization group simulations, we demonstrated that these states become energetically degenerate in the monoaxial limit, allowing the formation of magnetic Schrödinger cat states. We explored how the quantum skyrmion, antiskyrmion, and symmetric superposition states can be characterized through spin-spin correlation functions and their signatures in polarized neutron scattering. In particular, we found that the individual states display qualitative distinctions in theoretically calculated spin-flip SANS cross sections, which could serve as fingerprint observables for future experiments. Additionally, we investigate the coherent time evolution of the superposition state under a magnetic field gradient. Our results show spatial separation of the skyrmion and antiskyrmion components, in close agreement with semi-classical predictions based on Thiele's equation. Taken together, our findings establish a theoretical framework for the detection, manipulation, and potential control of skyrmionic Schrödinger cat states. They suggest that sufficient control over the DMI anisotropy and the gradient field can open up new avenues for quantum computation using quantum skyrmions as qubits.

ACKNOWLEDGMENTS

We acknowledge financial support from the Luxembourg National Research Fund under Grants No.

C22/MS/17415246/DeQuSky and No. AFR/23/17951349. V.M.K. acknowledges financial support from the European Union's Horizon Europe research and innovation programme under the Marie Skłodowska-Curie Grant Agreement No. 101203692 (QUANTHOPF).

DATA AVAILABILITY

The data that support the findings of this article were created using the ITensor software library and are openly available [76,77].

APPENDIX A: SIMULATIONS WITH DIPOLAR INTERACTIONS

To study the effect of dipolar fields on the skyrmion-antiskyrmion degeneracy point, we performed micromagnetic simulations of a 2D system using Mumax3 and the following material parameters: saturation magnetization $M_s = 384$ kA/m, exchange-stiffness constant $A = 4$ pJ/m, DMI constant $D = 0.785\,\mathrm{mJ/m^2}$, and an externally applied magnetic field of $B_z = 0.5$ T. The system size was chosen large enough to fit a skyrmion state ($L_x = L_y = 256\,\mathrm{nm}$), with a thickness of $L_z = 1\,\mathrm{nm}$ and a discretization (cuboid size) of 1 nm in all dimensions. While computing the demagnetizing kernel, we set periodic boundary conditions in the x-y plane with 50 repetitions in each direction. Starting with a skyrmion (antiskyrmion) state at $\alpha = 1$ ($\alpha = -1$), we have gradually decreased (increased) the DM anisotropy α and optimized the state. In this way, we have obtained the energies of skyrmion and antiskyrmion states for different α values, which are plotted in Fig. 6. As follows from these simulations, the degeneracy point is shifted towards negative values of α.

APPENDIX B: LOCAL FIDELITY

In addition to the local von Neumann entropy, one may introduce a number of observables to gauge the quantum nature of an MPS. To measure how closely a product state resembles an arbitrary MPS, we calculate the local fidelity, effectively quantifying local overlaps between a product state and an MPS. To do so, we construct the local projector onto the Pauli basis:

$$\hat{P}(\boldsymbol{m}_i) = \hat{P}_i = \frac{1}{2}\left(\mathbb{1} + \frac{\boldsymbol{m}_i \cdot \boldsymbol{\sigma}_i}{|\boldsymbol{m}_i|}\right), \tag{B1}$$

where $\boldsymbol{m}_i = \langle\psi|\hat{\boldsymbol{S}}_i|\psi\rangle$, $|\psi\rangle$ is the MPS and $\boldsymbol{\sigma}_i$ is the matrix of Pauli matrices on site i. We define local fidelity as the expectation value of $\hat{P}_i$, i.e., $\mathrm{Tr}(\hat{\rho}_i\hat{P}_i)$, where $\hat{\rho}_i = \mathrm{Tr}_{\bar{i}}\,|\psi\rangle\langle\psi|$ is the reduced density matrix. We present the local fidelity, the von Neumann entropy $S_i = -\mathrm{Tr}(\hat{\rho}_i \ln\hat{\rho}_i)$, and the magnetization norm $|\boldsymbol{m}_i|$ in Fig. 7. These local observables are calculated for monoaxial skyrmion and antiskyrmion MPS wave functions, their symmetric superposition, and a skyrmion MPS for a system with isotropic DMI ($\alpha = 1$). We observe that the entropy is bound to regions of noncollinear spins. For the isotropic DMI case in Figs. 7(a)–7(c), this region happens to be located at the perimeter of the axially symmetric skyrmion where the magnetization arrows lie in the xy plane. For the monoaxial DMI case, these regions are deformed into two spatially separate domains which accommodate the elliptical shape of the skyrmion texture. The suppressed fidelity regions coincide with regions with an increase in von Neumann entanglement entropy due to quantum fluctuations and regions with a reduced magnetization norm. This supports the statement that these observables, though not strictly equivalent, consistently indicate quantum behavior in a similar fashion.

APPENDIX C: SANS CROSS SECTIONS OF PRODUCT STATES

Calculating the SANS observables of product states allows us to gauge the neutron response of our matrix product states against responses of states that behave classically. We will proceed to show that a symmetric superposition of product states produces qualitatively the same signal as the MPS analog in a scattering observable that we dub the (un)polarized connected cross section:

$$\frac{d\Sigma^{\mathrm{C}}}{d\Omega} = \sum_{\alpha\beta}\left(\delta_{\alpha\beta} - \frac{q_\alpha q_\beta}{q^2}\right)\mathcal{S}^{\mathrm{C}}_{\alpha\beta}, \tag{C1}$$

where $\alpha, \beta \in \{x, y\}$ for the spin-flip SANS cross section, $\alpha, \beta \in \{x, y, z\}$ for the unpolarized cross section, and $q_z \approx 0$. In the calculation of the structure factors $\mathcal{S}^{\mathrm{C}}_{\alpha\beta}$, the calculation of two-point correlation functions becomes relevant. The matrix elements are given by

$$\langle\phi_{\mathrm{sk}}|\hat{\boldsymbol{S}}_i\hat{\boldsymbol{S}}_j|\phi_{\mathrm{ask}}\rangle = \langle\boldsymbol{n}_i|\hat{\boldsymbol{S}}_i|\overline{\boldsymbol{n}}_i\rangle\,\langle\boldsymbol{n}_j|\hat{\boldsymbol{S}}_j|\overline{\boldsymbol{n}}_j\rangle\prod_{k\neq i,j} v_k, \tag{C2}$$

and are also largely suppressed by the overlap elements v_k discussed in Sec. III C.

The structure factors for the connected cross section are defined as the Fourier transforms of the connected correlation $\Gamma^{\alpha\beta}_{ij} \equiv \langle\hat{S}_{i,\alpha}\hat{S}_{j,\beta}\rangle - \langle\hat{S}_{i,\alpha}\rangle\langle\hat{S}_{j,\beta}\rangle$:

$$\mathcal{S}^{\mathrm{C}}_{\alpha\beta} = \sum_{ij} e^{-\mathrm{i}\boldsymbol{q}\cdot(\boldsymbol{r}_i - \boldsymbol{r}_j)}\Gamma^{\alpha\beta}_{ij}, \tag{C3}$$

where the wave function is, in general, the superposition of the skyrmion and antiskyrmion product states, $|\phi\rangle = c\,|\phi_{\mathrm{ask}}\rangle + \sqrt{1-c^2}e^{\mathrm{i}\varphi}\,|\phi_{\mathrm{sk}}\rangle$. The diagonal elements $i = j$ in the transform yield a $\boldsymbol{q}$-independent contribution and therefore shall be ignored for now, as they only form a constant background on the level of the structure factors. The individual off-diagonal components read as

$$\Gamma^{\alpha\beta}_{ij} = \tfrac{1}{4}c^2(1-c^2)(n_{i,\alpha}n_{j,\beta} + \overline{n}_{i,\alpha}\overline{n}_{j,\beta} - n_{i,\alpha}\overline{n}_{j,\beta} - \overline{n}_{i,\alpha}n_{j,\beta}), \tag{C4}$$

where terms of the order $\prod_{k\neq i,j}|v_k|$ and smaller are neglected. It follows that in the case of exactly overlapping textures, the only nonvanishing contribution corresponds to $\alpha = \beta = y$ and reaches its maximum at $c^2 = 1/2$, which yields $\Gamma^{yy}_{ij} = \frac{1}{4}n_{i,y}n_{j,y}$. The Fourier transform of this connected part is solely responsible for the distinct Bragg peaks in the SANS signal of the equal-part superposition. In the case of displaced skyrmion and antiskyrmion textures, other structure factors become prominent.

Under the influence of the magnetic field gradient $\boldsymbol{B}^{\mathrm{grad}}$, the textures drift apart in opposite directions. The velocity $\boldsymbol{v}$ relative to the origin is calculated in Eq. (D14) for the

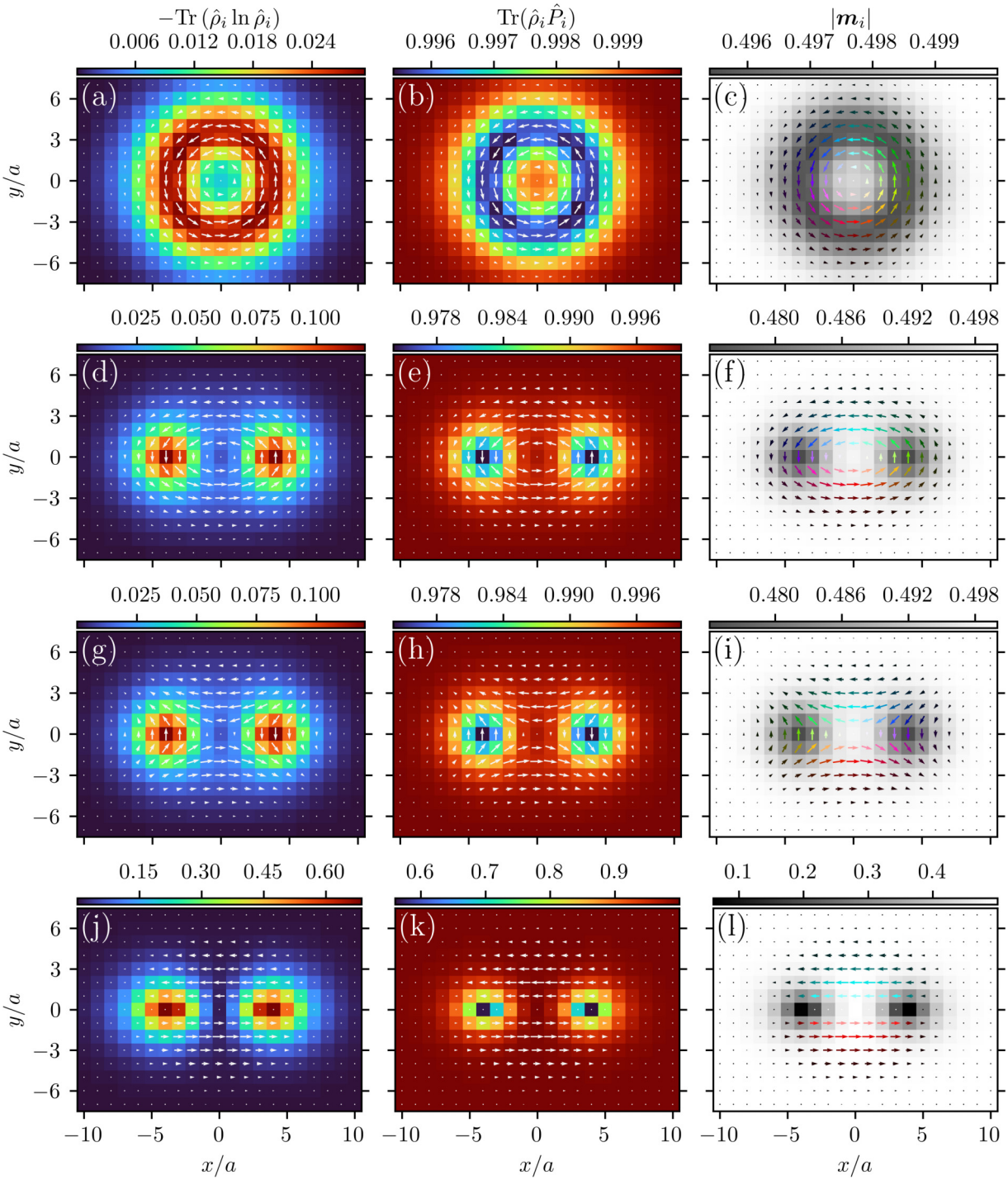

FIG. 7. (a)–(c) Spatial profiles of the von Neumann entropy, the local fidelity, and the magnetization norm, respectively, calculated for a skyrmion MPS obtained for an axially symmetric magnet ($\alpha = 1$). (d)–(f); (g)–(i) The same local observables for a skyrmion and antiskyrmion MPS in a monoaxial magnet, respectively. The last row (k)–(l) corresponds to the symmetric superposition of the skyrmion and antiskyrmion states. The used DMI strength is $D = J/2$ with $B = 0.8B_{\mathrm{D}}$ for the symmetric skyrmion and $B = 0.6B_{\mathrm{D}}$ for the monoaxial states.

continuum limit. Adopting a reference frame connected with the skyrmion texture, we write the Fourier components in the continuum limit as follows:

$$\begin{aligned}\Gamma^{\alpha\beta}(\boldsymbol{r},\boldsymbol{r}') = \tfrac{1}{4}c^2(1-c^2)[&n_\alpha(\boldsymbol{r})n_\beta(\boldsymbol{r}')\\ &+\overline{n}_\alpha(\boldsymbol{r})\overline{n}_\beta(\boldsymbol{r}'-n_\alpha)(\boldsymbol{r})\overline{n}_\beta(\boldsymbol{r}')\\ &-\overline{n}_\alpha(\boldsymbol{r})n_\beta(\boldsymbol{r}')].\end{aligned} \tag{C5}$$

Using the relation $\overline{\boldsymbol{n}}(\boldsymbol{r}) = \mathrm{diag}(1,-1,1)\boldsymbol{n}(\boldsymbol{r}-2\boldsymbol{v}t)$, we find that the structure factors inherit a time dependence

$$\begin{aligned}\mathcal{S}^{\mathrm{C}}_{yy} &= c^2(1-c^2)\cos^2(\boldsymbol{q}\cdot\boldsymbol{v}t)\mathcal{F}_{yy}(\boldsymbol{q}),\\ \mathcal{F}_{\alpha\beta}(\boldsymbol{q}) &= \int d^3r d^3r' e^{-\mathrm{i}\boldsymbol{q}\cdot(\boldsymbol{r}-\boldsymbol{r}')} n_\alpha(\boldsymbol{r})n_\beta(\boldsymbol{r}').\end{aligned} \tag{C6}$$

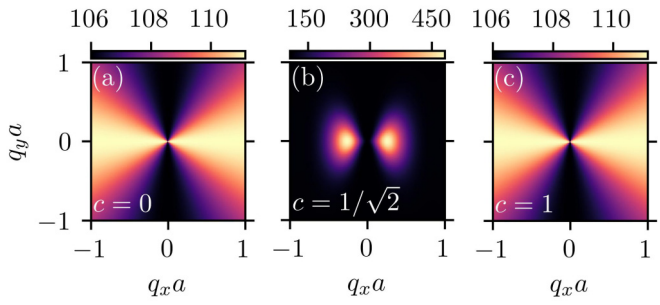

FIG. 8. The connected cross section $d\Sigma^{\mathrm{C}}/d\Omega$ of the skyrmion product state (a), antiskyrmion product state (c) and their symmetric superposition (b). Due to the relative sign flip of $n_{i,y}$ between the skyrmion and antiskyrmion textures, their SANS signals obtain opposite corrections in the subleading order. Since the amplitude of the corrections is small, (a) and (c) appear to be identical.

The structure factor above is predominant as long as $t \ll (\boldsymbol{q}\cdot\boldsymbol{v})^{-1}$. Analogously, $\mathcal{S}^{\mathrm{C}}_{xx}$ and $\mathcal{S}^{\mathrm{C}}_{zz}$ grow parabolically on this timescale, i.e.,

$$\mathcal{S}^{\mathrm{C}}_{\alpha\alpha} = c^2(1-c^2)\sin^2(\boldsymbol{q}\cdot\boldsymbol{v}t)\mathcal{F}_{\alpha\alpha}(\boldsymbol{q}), \tag{C7}$$

for $\alpha \in \{x, z\}$.

For the product states ($c \in \{0, 1\}$), the Fourier components $\Gamma^{\alpha\beta}_{ij}$ vanish under the assumption that $i \neq j$. In this case, the only contribution stems from the diagonal elements related to on-site correlations:

$$\mathcal{S}^{\mathrm{C}}_{\alpha\beta} = \sum_i \Big[\frac{1}{4}\delta_{\alpha\beta} - c^4\overline{n}_{i,\alpha}\overline{n}_{i,\beta} - (1-c^2)^2 n_{i,\alpha}n_{i,\beta} + \frac{\mathrm{i}}{2}\varepsilon_{\alpha\beta\gamma}(c^2\overline{n}_{i,\gamma} + (1-c^2)n_{i,\gamma})\Big], \tag{C8}$$

where we omitted the terms that vanish regardless whether $c = 0$ or $c = 1$. Moreover, due to the symmetric term $\delta_{\alpha\beta} - q_\alpha q_\beta$ in the cross section (C1), the antisymmetric complex term does not contribute to the final observable. These structure factors do not depend on the wave vector $\boldsymbol{q}$ and only contribute to the background.

Unlike the response of the skyrmion and antiskyrmion MPS, the connected cross sections of their product-state counterparts therefore show no significant structure. The cross sections of the individual product states and their symmetric superposition are shown in Fig. 8. The conical structure of the cross sections is present merely because of the term $q_\alpha q_\beta$ in the definition (C1).

APPENDIX D: SKYRMION DYNAMICS IN THE CLASSICAL LIMIT

Consider the following Hamiltonian with a perturbation in the form of a coordinate-dependent Zeeman term:

$$s\hat{H} = -\frac{1}{2}\sum_{\langle ij\rangle}[J\hat{\boldsymbol{S}}_i\cdot\hat{\boldsymbol{S}}_j + \boldsymbol{D}_{ij}\cdot(\hat{\boldsymbol{S}}_i\times\hat{\boldsymbol{S}}_j)] - \sum_i\left(\boldsymbol{B}+\boldsymbol{B}_i^{\mathrm{grad}}\right)\cdot\hat{\boldsymbol{S}}_i, \tag{D1}$$

where $\boldsymbol{B}_i^{\mathrm{grad}} = B_{\mathrm{grad}}\frac{2}{N_y-1}(0,0,y_i)$ is a gradient field with a small amplitude $|B_{\mathrm{grad}}| \ll |B|$. We employ the mean-field approximation to study how this perturbation induces the movement of topologically charged magnetic textures. With the assumption that the spins of the system are mutually weakly correlated, we construct an effective Hamiltonian by introducing the spin fluctuation from the mean value, $\delta\hat{\boldsymbol{S}}_i = \hat{\boldsymbol{S}}_i - \boldsymbol{m}_i$, where $\boldsymbol{m}_i = \langle\hat{\boldsymbol{S}}_i\rangle$. Plugging this into $\hat{H}$ and omitting second-order fluctuation terms, we obtain the mean-field non-interacting Hamiltonian:

$$s\hat{H} \approx s\hat{H}_{\mathrm{MF}} = -\sum_{\langle ij\rangle}[J\delta\hat{\boldsymbol{S}}_i\cdot\boldsymbol{m}_j + \boldsymbol{D}_{ij}\cdot\delta\hat{\boldsymbol{S}}_i\times\boldsymbol{m}_j] - \sum_i\left(\boldsymbol{B}+\boldsymbol{B}_i^{\mathrm{grad}}\right)\cdot\delta\hat{\boldsymbol{S}}_i + sE[\boldsymbol{m}], \tag{D2}$$

where the term $sE[\boldsymbol{m}]$ is proportional to the energy of the mean magnetization texture $\boldsymbol{m}$. As this term is not operator valued, it does not contribute to the spin dynamics and may be omitted. Furthermore, we assume that for negligible fluctuations, the texture has a uniform norm $|\boldsymbol{m}| = s$.

The time evolution of the spin operator $\hat{\boldsymbol{S}}_i$ in the Heisenberg picture is then determined via the commutator with the mean-field Hamiltonian,

$$\frac{\mathrm{d}}{\mathrm{d}t}\hat{\boldsymbol{S}}_i = \frac{i}{\hbar}[\hat{H}_{\mathrm{MF}}, \hat{\boldsymbol{S}}_i] = -\hat{\boldsymbol{S}}_i\times\boldsymbol{H}_i^{\mathrm{eff}}/s, \tag{D3}$$

$$\boldsymbol{H}_i^{\mathrm{eff}} = -\sum_{j\in\mathrm{NN}(i)}[J\boldsymbol{m}_j + \boldsymbol{m}_j\times\boldsymbol{D}_{ij}] - \boldsymbol{B} - \boldsymbol{B}_i^{\mathrm{grad}}. \tag{D4}$$

For the local observables, it follows that

$$\dot{\boldsymbol{m}}_i = -\boldsymbol{m}_i\times\boldsymbol{H}_i^{\mathrm{eff}}/s, \tag{D5}$$

which is the Landau-Lifshitz equation. Using the above equation, we can numerically resolve that topologically charged (anti)skyrmion domains display translational motion, with

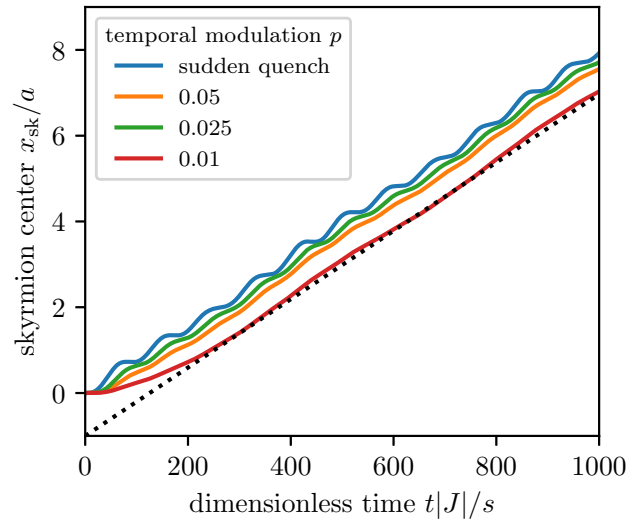

FIG. 9. Trajectories of the skyrmion center relaxed in a monoaxial chiral magnet under a gradient field perturbation. As the modulating function $\frac{2}{\pi}\arctan(\sinh(pt|J|/s))$ increases more slowly, the velocity approaches the analytical solution (D14).

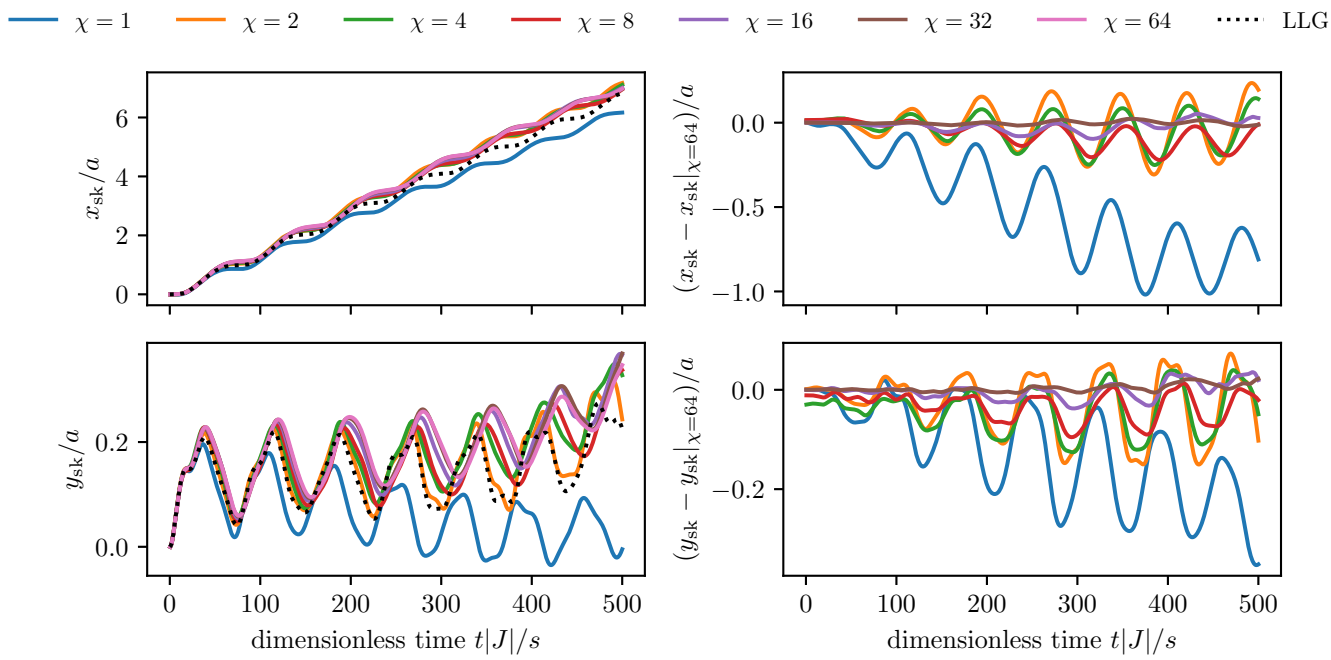

FIG. 10. TDVP results of the skyrmion motion x_{sk} and y_{sk} for different bond dimensions χ. For $\chi = 32$, the lines visually collapse with $\chi = 64$ over a large time window, with a maximum deviation $0.034a$ in x_{sk} and $0.022a$ in y_{sk}, respectively. The dashed line corresponds to the result from classical LLG simulations.

velocity perpendicular to the perturbation gradient. The Thiele equation reads

$$\boldsymbol{G} \times \boldsymbol{v} - \boldsymbol{F} = 0, \tag{D6}$$

where the gyrocoupling vector **G** and the force vector **F** are defined as

$$G_i = -\varepsilon_{ijk} \frac{1}{2s^2} \int \left[\boldsymbol{m} \cdot \left(\frac{\partial \boldsymbol{m}}{\partial x_j} \times \frac{\partial \boldsymbol{m}}{\partial x_k} \right) \right] dxdy, \tag{D7}$$

$$F_i = \frac{1}{s} \int \left[\boldsymbol{H}^{\text{eff}} \cdot \frac{\partial \boldsymbol{m}}{\partial x_i} \right] dxdy. \tag{D8}$$

For a skyrmion that is considered to be rigid, the internal forces related to exchange, Dzyaloshinskii-Moriya, and Zeeman interactions must be zero. The gradient field contributions for a $L_x \times L_y$ rectangular flake are

$$F_x = \frac{2B_{\text{grad}}}{sL_y} \int y \frac{\partial m_z}{\partial x} d^2r = \frac{2B_{\text{grad}}}{sL_y} \times \int_{-L_y/2}^{L_y/2} y \left[m_z\left(\frac{L_x}{2}, y\right) - m_z\left(-\frac{L_x}{2}, y\right) \right] dy = 0 \tag{D9}$$

and

$$F_y = \frac{2B_{\text{grad}}}{sL_y} \int y \frac{\partial m_z}{\partial y} d^2r = \frac{2B_{\text{grad}}}{sL_y} \times \int \underbrace{\left[\frac{L_y}{2} m_z\left(x, \frac{L_y}{2}\right) + \frac{L_y}{2} m_z\left(x, -\frac{L_y}{2}\right) \right]}_{sL_y} dx - \frac{2B_{\text{grad}}}{sL_y} \int m_z d^2r. \tag{D10}$$

We considered the edge magnetization to be fixed along the direction of the Zeeman field, $\boldsymbol{m}|_{\text{edge}} = s\boldsymbol{B}/|\boldsymbol{B}| = (0, 0, s)$. Equivalently, semiperiodic or periodic boundaries may be used. The nonvanishing force becomes

$$F_y = -\frac{2B_{\text{grad}}}{sL_y} \int (m_z - s) d^2r \equiv -\frac{2B_{\text{grad}}}{sL_y} N, \tag{D11}$$

where N is the total deviation of m_z from the amplitude s. For a domain with a rigid shape, N is constant in time.

As the z derivatives of the magnetization vanish, the only nonzero element of the gyrovector is G_z,

$$G_z = \frac{1}{s^2} \int \left[\boldsymbol{m} \cdot \left(\frac{\partial \boldsymbol{m}}{\partial y} \times \frac{\partial \boldsymbol{m}}{\partial x} \right) \right] dxdy = -4\pi Qs, \tag{D12}$$

where we used the formula for the topological charge defined for the unit vector field $\boldsymbol{n} = \boldsymbol{m}/s$:

$$Q = \frac{1}{4\pi} \int \left[\boldsymbol{n} \cdot \left(\frac{\partial \boldsymbol{n}}{\partial x} \times \frac{\partial \boldsymbol{n}}{\partial y} \right) \right] dxdy.$$

The Thiele equation then becomes

$$\begin{pmatrix} 4\pi Qsv_y \\ -4\pi Qsv_x \\ 0 \end{pmatrix} = \begin{pmatrix} 0 \\ -2B_{\text{grad}} N/(sL_y) \\ 0 \end{pmatrix}, \tag{D13}$$

with the solution

$$\boldsymbol{v} = \frac{B_{\text{grad}} N}{2\pi s^2 Q L_y} \boldsymbol{e}_x. \tag{D14}$$

The simulated velocity of the skyrmion can be compared with the analytical result (D14) obtained for the continuum limit.

We observe that the skyrmion trajectory displays oscillations about an average linear path in both the classical and quantum simulations. This comes from the sudden quench of

the gradient field, as it is effectively introduced as $B_{\mathrm{grad}}(t) \propto \Theta(t)$. We conclude that an abrupt jump in the amplitude of the perturbation excites other skyrmionic motion modes such as breathing or rotation modes on top of the linear translation. In Fig. 9, we show that the oscillations level out for $B_{\mathrm{grad}}(t)$ modulated by a slowly increasing smooth function. We choose to parametrize the gradient field with $(2/\pi)\arctan(\sinh(pt|J|/s))$ and vary p.

APPENDIX E: CONVERGENCE OF DMRG-X AND TDVP SIMULATIONS

We consider the dynamics of the approximate eigenstates of $\hat{H}$ by simulating the unitary evolution generated from the perturbed Hamiltonian $\hat{H}$. The best-effort converged DMRG-X states with $\chi = 16$ are used as the initial states of the TDVP algorithm. During simulation, we allow the bond dimension to increase to a maximum of $\chi = 64$. We exploit the exact relation $|\psi_{\mathrm{ask}}(t)\rangle = \hat{K}\,|\psi_{\mathrm{sk}}(-t)\rangle$ to simulate the antiskyrmion trajectory via the time-reversed skyrmion trajectory. The results for different bond dimensions are presented in Fig. 10. We find a visible collapse of the x_{sk} trajectory for $\chi \in \{16, 32, 64\}$ in the total time window, with a difference that consistently decreases when χ is increased. This trend is similar for y_{sk}. The DMRG-X states themselves are susceptible to the choice of the input states because DMRG-X seeks to maximize the fidelity of the result with the initial guess. However, we found that skyrmionlike initial states reliably converge to the same eigenstate regardless of their individual radii and eccentricities, provided they are entirely contained within the lattice. We conclude that all textures with lattice topological charge $Q \approx 1$ constitute appropriate initial states for the skyrmion, while the same holds for the antiskyrmion with $Q \approx -1$.

Moreover, we checked explicitly that changing the boundary conditions has little to no effect on the skyrmion state, provided that the skyrmion radius is sufficiently small compared to the lattice size. We found that open BC result in a chiral surface twist localized along the y boundary. The twist extends roughly six lattice sites into the system, and therefore approximately 12 additional sites are needed along y to host a skyrmion embedded in the modified polarized environment. Note that due to investigating monoaxial DMI, no surface twists appear along the x direction. In conclusion, simulating open or periodic boundary conditions does not show qualitative changes with respect to the bulk physics investigated in the present manuscript.

[1] Y. Tokura and N. Kanazawa, Magnetic skyrmion materials, Chem. Rev. **121**, 2857 (2021).

[2] K. M. Song, J.-S. Jeong, B. Pan, X. Zhang, J. Xia, S. Cha, T.-E. Park, K. Kim, S. Finizio, J. Raabe, J. Chang, Y. Zhou, W. Zhao, W. Kang, H. Ju, and S. Woo, Skyrmion-based artificial synapses for neuromorphic computing, Nat. Electron. **3**, 148 (2020).

[3] C. Psaroudaki, E. Peraticos, and C. Panagopoulos, Skyrmion qubits: Challenges for future quantum computing applications, Appl. Phys. Lett. **123**, 260501 (2023).

[4] J. Xia, X. Zhang, X. Liu, Y. Zhou, and M. Ezawa, Universal quantum computation based on nanoscale skyrmion helicity qubits in frustrated magnets, Phys. Rev. Lett. **130**, 106701 (2023).

[5] A. P. Petrović, C. Psaroudaki, P. Fischer, M. Garst, and C. Panagopoulos, *Colloquium*: Quantum properties and functionalities of magnetic skyrmions, Rev. Mod. Phys. **97**, 031001 (2025).

[6] E. M. Chudnovsky and D. A. Garanin, Magnetic skyrmion as Schrödinger's cat, Europhys. Lett. **151**, 46001 (2025).

[7] A. N. Bogdanov and D. A. Yablonskii, Thermodynamically stable "vortices" in magnetically ordered crystals. The mixed state of magnets, Sov. Phys. JETP **68** (1989).

[8] A. Bocdanov and A. Hubert, The properties of isolated magnetic vortices, Phys. Status Solidi B **186**, 527 (1994).

[9] I. Dzyaloshinsky, A thermodynamic theory of "weak" ferromagnetism of antiferromagnetics, J. Phys. Chem. Solids **4**, 241 (1958).

[10] T. Moriya, Anisotropic superexchange interaction and weak ferromagnetism, Phys. Rev. **120**, 91 (1960).

[11] H. Ochoa and Y. Tserkovnyak, Quantum skyrmionics, Int. J. Mod. Phys. B **33**, 1930005 (2019).

[12] V. Lohani, C. Hickey, J. Masell, and A. Rosch, Quantum skyrmions in frustrated ferromagnets, Phys. Rev. X **9**, 041063 (2019).

[13] O. M. Sotnikov, V. V. Mazurenko, J. Colbois, F. Mila, M. I. Katsnelson, and E. A. Stepanov, Probing the topology of the quantum analog of a classical skyrmion, Phys. Rev. B **103**, L060404 (2021).

[14] S. A. Díaz and D. P. Arovas, Quantum nucleation of skyrmions in magnetic films by inhomogeneous fields, in *Memorial Volume for Shoucheng Zhang* (World Scientific Connect, Singapore, 2021), Chap. 2, pp. 19–33.

[15] A. Haller, S. Groenendijk, A. Habibi, A. Michels, and T. L. Schmidt, Quantum skyrmion lattices in Heisenberg ferromagnets, Phys. Rev. Res. **4**, 043113 (2022).

[16] P. Siegl, E. Y. Vedmedenko, M. Stier, M. Thorwart, and T. Posske, Controlled creation of quantum skyrmions, Phys. Rev. Res. **4**, 023111 (2022).

[17] V. Vijayan, L. Chotorlishvili, A. Ernst, S. S. P. Parkin, M. I. Katsnelson, and S. K. Mishra, Topological dynamical quantum phase transition in a quantum skyrmion phase, Phys. Rev. B **107**, L100419 (2023).

[18] V. V. Mazurenko, I. A. Iakovlev, O. M. Sotnikov, and M. I. Katsnelson, Estimating patterns of classical and quantum skyrmion states, J. Phys. Soc. Jpn. **92**, 081004 (2023).

[19] R. Peters, J. Neuhaus-Steinmetz, and T. Posske, Quantum skyrmion Hall effect in f-electron systems, Phys. Rev. Res. **5**, 033180 (2023).

[20] A. Joshi, R. Peters, and T. Posske, Ground state properties of quantum skyrmions described by neural network quantum states, Phys. Rev. B **108**, 094410 (2023).

[21] O. M. Sotnikov, E. A. Stepanov, M. I. Katsnelson, F. Mila, and V. V. Mazurenko, Emergence of classical magnetic order from

Anderson towers: Quantum Darwinism in action, Phys. Rev. X **13**, 041027 (2023).

[22] A. Joshi, R. Peters, and T. Posske, Quantum skyrmion dynamics studied by neural network quantum states, Phys. Rev. B **110**, 104411 (2024).

[23] F. Salvati, M. I. Katsnelson, A. A. Bagrov, and T. Westerhout, Stability of a quantum skyrmion: Projective measurements and the quantum Zeno effect, Phys. Rev. B **109**, 064409 (2024).

[24] S. Sorn, J. Schmalian, and M. Garst, Topological dipoles of quantum skyrmions, Phys. Rev. X **15**, 041037 (2025).

[25] Z. Zhao, E. Östberg, F. Aryasetiawan, and C. Verdozzi, Quantum magnetic skyrmions on the Kondo lattice, Phys. Rev. Res. **7**L032012 (2025).

[26] R. Makuta and C. Hotta, Spin-orbit coupled Hubbard skyrmions, Phys. Rev. Res. **6**, 023133 (2024).

[27] S. A. Díaz, J. Klinovaja, D. Loss, and S. Hoffman, Majorana bound states induced by antiferromagnetic skyrmion textures, Phys. Rev. B **104**, 214501 (2021).

[28] J. Nothhelfer, S. A. Díaz, S. Kessler, T. Meng, M. Rizzi, Kjetil M. D. Hals, and K. Everschor-Sitte, Steering Majorana braiding via skyrmion-vortex pairs: A scalable platform, Phys. Rev. B **105**, 224509 (2022).

[29] K. Mæland and A. Sudbø, Quantum fluctuations in the order parameter of quantum skyrmion crystals, Phys. Rev. B **105**, 224416 (2022).

[30] K. Mæland and A. Sudbø, Quantum topological phase transitions in skyrmion crystals, Phys. Rev. Res. **4**, L032025 (2022).

[31] Y. Togawa, T. Koyama, K. Takayanagi, S. Mori, Y. Kousaka, J. Akimitsu, S. Nishihara, K. Inoue, A. S. Ovchinnikov, and J. Kishine, Chiral magnetic soliton lattice on a chiral helimagnet, Phys. Rev. Lett. **108**, 107202 (2012).

[32] V. M. Kuchkin and N. S. Kiselev, Skyrmions and antiskyrmions in monoaxial chiral magnets, Phys. Rev. B **108**, 054426 (2023).

[33] V. M. Kuchkin and N. S. Kiselev, Turning a chiral skyrmion inside out, Phys. Rev. B **101**, 064408 (2020).

[34] F. Zheng, N. S. Kiselev, L. Yang, V. M. Kuchkin, F. N. Rybakov, S. Blügel, and R. E. Dunin-Borkowski, Skyrmion-antiskyrmion pair creation and annihilation in a cubic chiral magnet, Nat. Phys. **18**, 863 (2022).

[35] L. Li, D. Song, W. Wang, F. Zheng, A. Kovács, M. Tian, R. E. Dunin-Borkowski, and H. Du, Transformation from magnetic soliton to skyrmion in a monoaxial chiral magnet, Adv. Mater. **35**, 2209798 (2023).

[36] Y. Nabei, D. Hirobe, Y. Shimamoto, K. Shiota, A. Inui, Y. Kousaka, Y. Togawa, and H. M. Yamamoto, Current-induced bulk magnetization of a chiral crystal $CrNb_3S_6$, Appl. Phys. Lett. **117**, 052408 (2020).

[37] A. Inui, R. Aoki, Y. Nishiue, K. Shiota, Y. Kousaka, H. Shishido, D. Hirobe, M. Suda, J.-i. Ohe, J.-i. Kishine, H. M. Yamamoto, and Y. Togawa, Chirality-induced spin-polarized state of a chiral crystal $CrNb_3S_6$, Phys. Rev. Lett. **124**, 166602 (2020).

[38] S. K. Karna, F. N. Womack, R. Chapai, D. P. Young, M. Marshall, W. Xie, D. Graf, Y. Wu, H. Cao, L. DeBeer-Schmitt, P. W. Adams, R. Jin, and J. F. DiTusa, Consequences of magnetic ordering in chiral $Mn_{1/3}NbS_2$, Phys. Rev. B **100**, 184413 (2019).

[39] S. K. Karna, M. Marshall, W. Xie, L. DeBeer-Schmitt, D. P. Young, I. Vekhter, W. A. Shelton, A. Kovács, M. Charilaou, and J. F. DiTusa, Annihilation and control of chiral domain walls with magnetic fields, Nano Lett. **21**, 1205 (2021).

[40] C. Zhang, J. Zhang, C. Liu, S. Zhang, Y. Yuan, P. Li, Y. Wen, Z. Jiang, B. Zhou, Y. Lei, D. Zheng, C. Song, Z. Hou, W. Mi, U. Schwingenschlögl, A. Manchon, Z. Q. Qiu, H. N. Alshareef, Y. Peng, and X.-X. Zhang, Chiral helimagnetism and one-dimensional magnetic solitons in a Cr-intercalated transition metal dichalcogenide, Adv. Mater. **33**, 2101131 (2021).

[41] S. Mankovsky, S. Polesya, H. Ebert, and W. Bensch, Electronic and magnetic properties of $2H - NbS_2$ intercalated by $3d$ transition metals, Phys. Rev. B **94**, 184430 (2016).

[42] D. A. Mayoh, J. Bouaziz, A. E. Hall, J. B. Staunton, M. R. Lees, and G. Balakrishnan, Giant topological and planar Hall effect in $Cr_{1/3}NbS_2$, Phys. Rev. Res. **4**, 013134 (2022).

[43] M. Hoffmann, B. Zimmermann, G. P. Müller, D. Schürhoff, N. S. Kiselev, C. Melcher, and S. Blügel, Antiskyrmions stabilized at interfaces by anisotropic Dzyaloshinskii-Moriya interactions, Nat. Commun. **8**, 308 (2017).

[44] Q. Yang, Y. Cheng, Y. Li, Z. Zhou, J. Liang, X. Zhao, Z. Hu, R. Peng, H. Yang, and M. Liu, Voltage control of skyrmion bubbles for topological flexible spintronic devices, Adv. Electron. Mater. **6**, 2000246 (2020).

[45] L. Caretta, E. Rosenberg, F. Büttner, T. Fakhrul, P. Gargiani, M. Valvidares, Z. Chen, P. Reddy, D. A. Muller, C. A. Ross, and G. S. D. Beach, Interfacial Dzyaloshinskii-Moriya interaction arising from rare-earth orbital magnetism in insulating magnetic oxides, Nat. Commun. **11**, 1090 (2020).

[46] S. Ghosh, H. Katsumoto, G. Bihlmayer, M. Sallermann, V. M. Kuchkin, F. N. Rybakov, O. Eriksson, S. Blügel, and N. S. Kiselev, Linked skyrmions in shifted magnetic bilayer, Commun. Phys. **9**, 104 (2026).

[47] D. Bhowmick, A. Haller, D. S. Kathyat, T. L. Schmidt, and P. Sengupta, Quantum skyrmion liquid, Phys. Rev. B **111**, 134410 (2025).

[48] A. Haller, S. A. Díaz, W. Belzig, and T. L. Schmidt, Quantum magnetic skyrmion operator, Phys. Rev. Lett. **133**, 216702 (2024).

[49] V. M. Kuchkin, A. Haller, S. Liscak, M. P. Adams, V. Rai, E. P. Sinaga, A. Michels, and T. L. Schmidt, Quantum and classical magnetic Bloch points, Phys. Rev. Res. **7**, 013195 (2025).

[50] V. Khemani, F. Pollmann, and S. L. Sondhi, Obtaining highly excited eigenstates of many-body localized Hamiltonians by the density matrix renormalization group approach, Phys. Rev. Lett. **116**, 247204 (2016).

[51] S. R. White, Density matrix formulation for quantum renormalization groups, Phys. Rev. Lett. **69**, 2863 (1992).

[52] D. Perez-Garcia, F. Verstraete, M. Wolf, and J. Cirac, Matrix product state representations, Quantum Inf. Comput. **7**, 401 (2007).

[53] A. A. Thiele, Steady-state motion of magnetic domains, Phys. Rev. Lett. **30**, 230 (1973).

[54] S. Mühlbauer, D. Honecker, E. A. Périgo, F. Bergner, S. Disch, A. Heinemann, S. Erokhin, D. Berkov, C. Leighton, M. R. Eskildsen, and A. Michels, Magnetic small-angle neutron scattering, Rev. Mod. Phys. **91**, 015004 (2019).

[55] D. Honecker, M. Bersweiler, S. Erokhin, D. Berkov, K. Chesnel, D. A. Venero, A. Qdemat, S. Disch, J. K. Jochum, A. Michels, and P. Bender, Using small-angle scattering to

guide functional magnetic nanoparticle design, Nanoscale Adv. **4**, 1026 (2022).

[56] M. Kataoka, Spin waves in systems with long period helical spin density waves due to the antisymmetric and symmetric exchange interactions, J. Phys. Soc. Jpn. **56**, 3635 (1987).

[57] S. V. Grigoriev, A. S. Sukhanov, E. V. Altynbaev, S.-A. Siegfried, A. Heinemann, P. Kizhe, and S. V. Maleyev, Spin waves in full-polarized state of Dzyaloshinskii-Moriya helimagnets: Small-angle neutron scattering study, Phys. Rev. B **92**, 220415(R) (2015).

[58] J. Haegeman, C. Lubich, I. Oseledets, B. Vandereycken, and F. Verstraete, Unifying time evolution and optimization with matrix product states, Phys. Rev. B **94**, 165116 (2016).

[59] S. Paeckel, T. Köhler, A. Swoboda, S. R. Manmana, U. Schollwöck, and C. Hubig, Time-evolution methods for matrix-product states, Ann. Phys. **411**, 167998 (2019).

[60] S. Mühlbauer, B. Binz, F. Jonietz, C. Pfleiderer, A. Rosch, A. Neubauer, R. Georgii, and P. Böni, Skyrmion lattice in a chiral magnet, Science **323**, 915 (2009).

[61] X. Z. Yu, Y. Onose, N. Kanazawa, J. H. Park, J. H. Han, Y. Matsui, N. Nagaosa, and Y. Tokura, Real-space observation of a two-dimensional skyrmion crystal, Nature (London) **465**, 901 (2010).

[62] K. Shibata, A. Kovács, N. S. Kiselev, N. Kanazawa, R. E. Dunin-Borkowski, and Y. Tokura, Temperature and magnetic field dependence of the internal and lattice structures of skyrmions by off-axis electron holography, Phys. Rev. Lett. **118**, 087202 (2017).

[63] F. N. Rybakov, A. B. Borisov, S. Blügel, and N. S. Kiselev, New type of stable particlelike states in chiral magnets, Phys. Rev. Lett. **115**, 117201 (2015).

[64] V. M. Kuchkin, P. F. Bessarab, and N. S. Kiselev, Thermal generation of droplet soliton in chiral magnet, Phys. Rev. B **105**, 184403 (2022).

[65] V. M. Kuchkin, N. S. Kiselev, A. Haller, S. Liščák, A. Michels, and T. L. Schmidt, Stability and nucleation of dipole strings in uniaxial chiral magnets, Phys. Rev. B **111**, 174410 (2025).

[66] K. Gerlinger, B. Pfau, F. Büttner, M. Schneider, L.-M. Kern, J. Fuchs, D. Engel, C. M. Günther, M. Huang, I. Lemesh, L. Caretta, A. Churikova, P. Hessing, C. Klose, C. Strüber, C. v. K. Schmising, S. Huang, A. Wittmann, K. Litzius, D. Metternich, *et al.*, Application concepts for ultrafast laser-induced skyrmion creation and annihilation, Appl. Phys. Lett. **118**, 192403 (2021).

[67] L.-M. Kern, B. Pfau, V. Deinhart, M. Schneider, C. Klose, K. Gerlinger, S. Wittrock, D. Engel, I. Will, C. M. Günther, R. Liefferink, J. H. Mentink, S. Wintz, M. Weigand, M.-J. Huang, R. Battistelli, D. Metternich, F. Büttner, K. Höflich, and S. Eisebitt, Deterministic generation and guided motion of magnetic skyrmions by focused He^+-ion irradiation, Nano Lett. **22**, 4028 (2022).

[68] L. Powalla, M. T. Birch, K. Litzius, S. Wintz, F. Schulz, M. Weigand, T. Scholz, B. V. Lotsch, K. Kern, G. Schütz, and M. Burghard, Single skyrmion generation via a vertical nanocontact in a 2D magnet-based heterostructure, Nano Lett. **22**, 9236 (2022).

[69] L.-M. Kern, V. M. Kuchkin, V. Deinhart, C. Klose, T. Sidiropoulos, M. Auer, S. Gaebel, K. Gerlinger, R. Battistelli, S. Wittrock, T. Karaman, M. Schneider, C. M. Günther, D. Engel, I. Will, S. Wintz, M. Weigand, F. Büttner, K. Höflich, S. Eisebitt, *et al.*, Controlled formation of skyrmion bags, Adv. Mater. **37**, 2501250 (2025).

[70] E. Viñas Boström, A. Rubio, and C. Verdozzi, Microscopic theory of light-induced ultrafast skyrmion excitation in transition metal films, npj Comput. Mater. **8**, 62 (2022).

[71] L. Desplat, S. Meyer, J. Bouaziz, P. M. Buhl, S. Lounis, B. Dupé, and P.-A. Hervieux, Mechanism for ultrafast electric-field driven skyrmion nucleation, Phys. Rev. B **104**, L060409 (2021).

[72] K. T. Gahagan and G. A. Swartzlander, Optical vortex trapping of particles, Opt. Lett. **21**, 827 (1996).

[73] N. B. Simpson, K. Dholakia, L. Allen, and M. J. Padgett, Mechanical equivalence of spin and orbital angular momentum of light: An optical spanner, Opt. Lett. **22**, 52 (1997).

[74] H. Fujita and M. Sato, Ultrafast generation of skyrmionic defects with vortex beams: Printing laser profiles on magnets, Phys. Rev. B **95**, 054421 (2017).

[75] E. M. Chudnovsky and J. Tejada, *Macroscopic Quantum Tunneling of the Magnetic Moment* (Cambridge University Press, Cambridge, 1998).

[76] M. Fishman, S. R. White, and E. M. Stoudenmire, The ITensor software library for tensor network calculations, SciPost Phys. Codebases 4 (2022).

[77] S. Liscak, A. Haller, A. Michels, T. L. Schmidt, and V. M. Kuchkin, Data and code supplement: Skyrmionic Schrödinger cat states in monoaxial chiral magnets, Zenodo (2025), https://doi.org/10.5281/zenodo.17360498.